

USE OF PHOTON DETECTION TO OBTAIN
A CLEAN $\pi^+\pi^-\pi^0$ SIGNAL
FROM $\bar{p}p$ ANNIHILATIONS

by

Joseph L. Mildenberger
B.Sc., University of Victoria, Victoria, B.C., 1984

A THESIS SUBMITTED IN PARTIAL FULFILLMENT
OF THE REQUIREMENTS FOR THE DEGREE OF
MASTER OF SCIENCE

in the
Department of Physics

We accept this thesis as conforming
to the required standard:

ACCEPTED
FACULTY OF GRADUATE STUDIES
DATE 6, October, 1987 DEAN

Supervisor Dr. G.A. Beer

Dr. R.K. Keeler

Dr. D.J. Leeming

External examiner Dr. F. Ruskey

©JOSEPH L. MILDENBERGER, 1987
UNIVERSITY OF VICTORIA

*All rights reserved. This dissertation may not be reproduced
in whole or in part, by xerography or other means,
without the permission of the author.*

QC 793.5

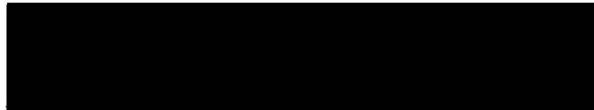
P728 M56

Abstract

Supervisor: Professor G. A. Beer

The availability of photon position information in the ASTERIX experiment has allowed the extraction of a very-nearly pure $\pi^+\pi^-\pi^0$ signal from $\bar{p}p$ annihilations at rest in a gaseous H_2 target. The conversion coordinates of the γ -rays from the decay of the π^0 enable a three-constraint (3C) kinematic fit to be performed on candidate events. The extra constraints serve to almost totally eliminate the background events, consisting mainly of $\pi^+\pi^-2\pi^0$ and $\pi^+\pi^-3\pi^0$ events. Monte Carlo simulations which take into account the momentum resolution for charged particles produce a missing-mass spectrum which agrees very well with the fit data. This is an improvement over data selected with a one-constraint (1C) kinematic fit, for which the level of contamination is estimated at $\approx 14\%$. Such a clean set of $\pi^+\pi^-\pi^0$ events should allow a more reliable and accurate amplitude-phase analysis to be done on the $\pi^+\pi^-\pi^0$ channel. This technique is also applicable to other channels with neutral particles that decay to γ -rays.

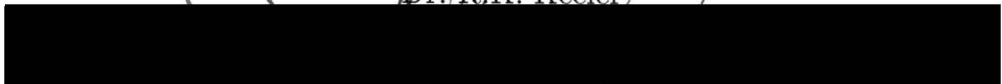
Examiners:



Supervisor Dr. G.A. Beer



Dr. R.K. Keeler



Dr. D.J. Leeming



Dr. F. Ruskey

Contents

Abstract	ii
Table of Contents	iii
List of Tables	iv
List of Figures	v
Acknowledgements	viii
Dedication	ix
1 Antiproton-Proton Physics at Rest	1
1.1 Previous Experiments	1
1.2 Physics with Low-Energy Antiprotons	3
1.3 Taking Advantage of LEAR	4
2 Goals of ASTERIX	6
2.1 Protonium Spectroscopy	6
2.2 Annihilation Dynamics	8
2.3 Bound States and Exotic Resonances	8
3 The ASTERIX Detector	10
3.1 Overview	10
3.2 Target and XDC	12
3.3 Magnetic Spectrometer	15
3.4 γ -ray Detection	19
3.5 Tracking	21
4 Analysis of $\pi^+\pi^-\pi^0$ Events	23
4.1 Significance	23

4.2	Aims of Analysis	24
4.3	Tracking of $\pi^+\pi^-\pi^0$ Events	24
4.4	Kinematic Fitting	26
4.5	Data Set Criteria	30
5	Results of Analysis	33
5.1	Effects of Cuts Prior to Fitting	33
5.2	$(M_{missing}^2)_{\pi^+\pi^-}$ Plots	35
5.3	Monte Carlo Simulations	37
5.4	Why the 3C-Fit Works	43
5.5	Detector Performance	47
5.6	Physics Results	54
5.7	Dalitz Plots	57
5.8	Invariant Mass Plots	61
5.9	Angular Distributions	62
5.10	X-ray Information	65
5.11	Further Prospects	67
	References	68

List of Tables

3.1	Characteristics of Cylindrical MWPC's	18
3.2	Characteristics of Endcap γ Detectors	20
5.1	Statistics for October 1985 2-Prong Data	35
5.2	G -parity conserving initial and intermediate states	56

List of Figures

3.1	Schematic diagram of ASTERIX Detector (side and front views)	10
3.2	Side view of target and XDC assembly	12
3.3	Schematic diagram of XDC (end view)	14
3.4	Schematic diagram of XDC (oblique view)	14
3.5	X-Ray event in XDC	15
3.6	Cosmic ray traversing XDC	16
3.7	Cosmic ray traversing two opposite cells of XDC	16
3.8	Positioning of MWPC's	17
3.9	Cut-away view of Q ₁ MWPC	18
3.10	Endcap PSGD configuration	20
5.1	\bar{p} z stopping distribution	34
5.2	$(M^2_{missing})_{\pi^+\pi^-}$ distribution from bubble chamber data . . .	37
5.3	$(M^2_{missing})_{\pi^+\pi^-}$ distribution and Monte Carlo approximation for fit events ($\chi^2 \leq 10$)	38
5.4	$(M^2_{missing})_{\pi^+\pi^-}$ distribution and Monte Carlo approximation for complete data set	39
5.5	$(M^2_{missing})_{\pi^+\pi^-}$ distribution and Monte Carlo approximation for fit events ($\chi^2 \leq 30$)	40
5.6	$(M^2_{missing})_{\pi^+\pi^-}$ distribution and Monte Carlo approximation for fit events ($\chi^2 \leq 100$)	41

5.7	χ^2 distribution for fit events	42
5.8	Monte Carlo simulation of γ -rays from $\pi^+\pi^-\pi^0$ events . . .	45
5.9	Monte Carlo simulation of γ -rays from $\pi^+\pi^-2\pi^0$ events . . .	45
5.10	Monte Carlo simulation of γ -rays from $\pi^+\pi^-3\pi^0$ events . . .	46
5.11	Initial value of sum of constraints	49
5.12	Initial value of sum of constraints (expanded)	49
5.13	$(M_{missing}^2)_{\pi^+\pi^-}$ distribution for events with $S_{initial} \geq 1.6$. . .	50
5.14	Charged-particle energy before and after fitting ($\chi^2 \leq 100$)	51
5.15	Charged-particle energy before and after fitting ($\chi^2 \leq 30$) .	51
5.16	Charged-particle energy before and after fitting ($\chi^2 \leq 10$) .	52
5.17	γ -ray z conversion distribution	53
5.18	γ -ray x - y conversion distribution	54
5.19	Dalitz plot from bubble chamber data	60
5.20	Dalitz plot from ASTERIX 3C fit	60
5.21	$(M_{inv}^2)_{\pi^+\pi^-}$ from ASTERIX 3C data	62
5.22	M_{inv}^2 plots from bubble chamber data	63
5.23	$(M_{inv}^2)_{\pi^+\pi^0}$ plot from ASTERIX 3C data	64
5.24	$(M_{inv}^2)_{\pi^-\pi^0}$ plot from ASTERIX 3C data	64
5.25	Angular distribution for positive dipion	65
5.26	Angular distribution for negative dipion	66
5.27	Angular distribution for neutral dipion	66

Acknowledgements

I would like to thank Dr. Beer for taking me on as a graduate student, with all that it implies. I would also like to thank Dr. E.G. Auld of UBC for assisting me in many aspects of this project, and Dr. R.K. Keeler for patiently answering so many of my physics questions along the way.

Dedication

To the memory of Shiming Li (1949–1987).

Chapter 1

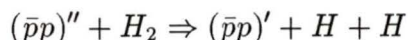
Antiproton-Proton Physics at Rest

1.1 Previous Experiments

Previous experiments involving antiproton-proton ($\bar{p}p$) annihilation at rest were performed almost exclusively in bubble chambers. These experiments typically had low statistics due mainly to the difficulty of producing large numbers of \bar{p} 's, combined with the low rate of data acquisition that is a fundamental characteristic of such a detector. There was also no capability to measure directly the initial angular momentum state of the $\bar{p}p$ system. These were two very important limitations, the former because of the large number of final states that are possible, and the latter because of the difficulty of determining which channels contribute to a given final state [1].

The use of liquid targets also had some other significant drawbacks. In order to understand what these are it is necessary to examine the processes by which protonium (a bound $\bar{p}p$ system) is formed and subsequently annihilated. An incident antiproton is captured in the Coulombic field of a hydrogen nucleus (a proton) by the Auger process, in which the electron orbiting the proton is ejected, and replaced by the antiproton. The most probable energy level for the \bar{p} to occupy upon first being captured is given

by $n_c = (M/m)^{1/2} \approx 30$ [2], where M and m are the reduced masses of the protonium atom and the hydrogen atom, respectively. If the protonium atom were in a vacuum it would de-excite radiatively with a mean lifetime of $\approx 10^{-7}$ s, until it reached (preferentially) the 3d or 2p level, when the probability of annihilation becomes much greater than the probability of further radiative de-excitations. The external effects of other hydrogen molecules cause several important deviations from this idealized scenario. The transitions for the higher states ($n \approx 30$ to $n \approx 20$) are primarily due to dissociations of neighboring H_2 molecules:



After this ($n \approx 20$ to $n \approx 5$) the dominant process is the ejection of Auger electrons from the neighboring molecules. It is only after the $\bar{p}p$ system has reached these relatively low levels that radiative de-excitations become prominent. As the frequency of collisions is a pressure-dependent parameter, the onset of domination by radiative transitions is lower ($n \approx 3$) in a liquid target than in a gaseous target [1]. This allows a much greater probability for detecting X-rays from the radiative transitions in a gaseous target. This was confirmed experimentally by the observation of X-rays from pionic hydrogen atoms (π^-p) in a gaseous target [3] and the failure to observe them in a liquid target [4].

Another important feature of liquid targets that places severe constraints on the study of $\bar{p}p$ annihilations is Stark mixing, which occurs when the neutral $\bar{p}p$ system (which is very small in relation to atomic distances) drifts into the Coulomb field of a neighboring proton. The electric field causes a mixing of states with the same principal quantum number n but with different orbital angular momentum quantum numbers l . If only radiative transitions occurred (i.e. in a vacuum), the system would preferentially occupy states with maximum angular momentum $l = n - 1$. As the $\bar{p}p$ system can annihilate from S- or P-states ($l = 0$ or $l = 1$, respectively)

with high n , we again have a great reduction in the number of X-rays and so have no direct knowledge of the angular momentum state from which annihilation occurred. As well, since S-wave annihilation is much more probable for states with high n [5] (although P-wave annihilations are more probable for low n [6]), certain rare final states such as $K_s^0 K_s^0$ and $\pi^0 \pi^0$ which are forbidden from S-wave annihilations were not observed, or if they were it was with very low statistics.

Bubble chambers as detectors had yet another important shortcoming: their efficiency for detecting neutral particles such as γ -rays (photons) from π^0 decay was very poor, as only charged particles leave tracks in the bubble chambers and the probability of the high-energy photons to interact with the target was very small.

1.2 Physics with Low-Energy Antiprotons

The Low Energy Antiproton Ring (LEAR) at CERN in Geneva, Switzerland is a unique facility for studying low-energy $\bar{p}p$ interactions. By the use of stochastic cooling, the ring is able to circulate large quantities ($\approx 10^{11}$) of low-momentum ($p_{min} \approx 100 MeV/c$) \bar{p} 's [7] with a low momentum spread ($\Delta p/p \approx \pm 1.1\%$) [8]¹. The availability of such large numbers of low-energy \bar{p} 's has made possible a number of new and important investigations into the fundamental properties of $\bar{p}p$ interactions. These include:

- Searches for new $\bar{p}p$ bound states or resonances, so-called “exotic” two, four and six-quark bound states, “glueballs” (bound systems of gluons) and other bound states predicted by theory;
- Spectroscopy of $\bar{p}p$ system: energy levels of bound systems, studied by measuring the energies and widths of the excited states. For the $\bar{p}p$ system, this includes the effects of the strong interaction on the

¹This figure has since been significantly improved to $\approx \pm 0.2\%$ [9].

coulombic energy levels through the shifting and broadening of the spectral lines as compared with their values calculated according to quantum electrodynamics (QED);

- Identification of as many of the available final states as possible, and accurate determinations of the relative probabilities (branching ratios) of different final states, and their correlations with the initial state of the $\bar{p}p$ system.

All of these investigations are essential to the understanding of the dynamics of the $\bar{p}p$ interaction at low energy. Ultimately it is hoped to be able to describe the interactions in terms of the constituents of the \bar{p} and the nucleon, that is the quarks and gluons. This knowledge will compliment the understanding of the so-called “parton” model that has emerged from experiments at very high energies, since the strong interaction is known to have different characteristics at different energies.

1.3 Taking Advantage of LEAR

The availability of copious quantities of low-energy antiprotons has allowed the construction of detectors that combine low-density targets, such as gaseous hydrogen (H_2) at a pressure of one atmosphere, with almost complete stopping efficiency. To take advantage of this very high stop rate requires a detector that is capable of observing $\bar{p}p$ interactions at a rate several orders of magnitude greater than is possible with a bubble chamber system. We can also enumerate several other characteristics that would be desirable in a detector to study $\bar{p}p$ interactions:

- As mentioned previously, we would like to be able to determine the state from which annihilation occurs. This would be possible if we could somehow observe and identify the X-rays that are emitted as the $\bar{p}p$ systems drop from higher to lower energy levels. Of particular

interest is the last X-ray that is observed, as this would determine the state from which annihilation occurs².

- We would like to have a high efficiency for charged-particle track detection, and good spatial resolution to enable high precision momentum determination.
- The solid angle subtended by the detector must be great enough to ensure that a minimum of information “leaks out”; in particular, it is important that charged particles not be missed.
- The ability to detect high-energy γ -rays is desirable to accurately identify and “reconstruct” many different final states that include neutral pions or other particles that (ultimately) have γ 's among their decay products.

These and other features were incorporated into the ASTERIX³ detector. The aims of ASTERIX will be discussed in more detail in Chapter 2. Chapter 3 will provide a description of the construction, operation, capabilities and limitations of the ASTERIX detector. In Chapter 4 the $\pi^+\pi^-\pi^0$ decay channel and the methods used for the identification, fitting and analysis of $\pi^+\pi^-\pi^0$ events will be examined, while Chapter 5 will discuss the results of the analysis and their significance to future work in this area.

²Assuming that no additional transitions, with either undetected X-rays, or non-radiative, occur

³Antiproton S**T**op Experiment with t**R**igger on Initial X-rays

Chapter 2

Goals of ASTERIX

2.1 Protonium Spectroscopy

The protonium atom ($\bar{p}p$) is similar in many respects to the ordinary hydrogen atom (H). It is a two-body system bound together by a Coulombic potential. Calculations can be done to determine the energy levels of the system in exactly the same manner as is done for the hydrogen atom, that is, by using the relativistic Dirac equation¹, but with the mass of the electron (e) replaced by that of the antiproton (\bar{p}). The mass difference between the e and the \bar{p} results in the expectation values for the radius of the $\bar{p}p$ system to be much smaller than that of the H atom. Since the \bar{p} is most likely to be captured at a radius corresponding to $n \approx 30$, which is the ground state radius of the hydrogen atom, of the order of 10^{-8} cm. At this radius the system is described very well by the Dirac equation because the separation of the p and \bar{p} is several orders of magnitude greater than the range of the hadronic (strong) interaction. As de-excitation occurs the wave functions of the p and \bar{p} begin to overlap more and more until the system reaches the 3d or 2p states from which more than 90% of the annihilations occur [2].

¹There is some controversy as to whether a $\bar{p}p$ system should be treated as a system of fermions, or as a single boson, in which case the Dirac equation would not be applicable. The observation of hyperfine splitting between different angular momentum states, if it is indeed observed, would justify the use of the Dirac equation.

The strong interaction produces two very important effects which manifest in the X-ray spectrum from the radiative transitions for low values of n ($n \leq 4$):

1. The energies of the X-rays will be shifted (ΔE) due to the attraction or repulsion of the hadronic forces.
2. The widths of the energy levels will be broadened ($\Delta\Gamma$) because of the shorter length of time (on average) that the system occupies a state due to annihilations.

These quantities provide important information about the dynamics of the hadronic interactions within the $\bar{p}p$ system. In particular, ΔE_{1s} and $\Delta\Gamma_{1s}$ are sensitive to $\bar{p}p$ resonances and hadronic $\bar{p}p$ states with masses less than $2m_p$ [10], where m_p is the mass of the proton. Previous to the ASTERIX results [9] there were no direct measurements of these quantities because the K X-ray line for protonium had not been clearly observed, although L X-rays had been observed in several experiments².

Theory predicts that there will be hyperfine splitting between the spin triplet and spin singlet ground states of the protonium atom [11], i.e. the energy shifts and broadening due to the hadronic force will be different for transitions to the 1^3S_1 and 1^1S_0 states. Because the difference in energy shifts is expected to be only ≈ 200 eV and the widths of the lines ≈ 1000 eV [10], a separate determination of the shifts and broadenings would likely be very difficult if only the energies of the measured X-rays were to be taken into account. But the ASTERIX spectrometer, by selecting final states which are unique to either the triplet or singlet ground state of the protonium atom, enables the transitions to the different states to be examined separately: the decay $\bar{p}p \rightarrow \pi^+\pi^-$ can occur from the triplet state only, so that K_α X-rays detected in coincidence with back-to-back charged pions will indicate that the transition was to the triplet state.

²See for example reference [6].

2.2 Annihilation Dynamics

The results from bubble chamber experiments indicate that in liquid H_2 targets annihilations occur most frequently from high n S-states. Indeed, only the very rare $\pi^0\pi^0$ events provide any evidence at all that annihilation can occur from P-states [12]. In gas targets P-wave annihilation becomes much more frequent. If the cascade reaches the 2p level annihilations occur in more than 90% of the cases while K_α X-rays are radiated in less than 10% of the cases [6]. Calculations that attempt to describe the cascade processes suggest that at a pressure of one atmosphere the frequencies of S-wave and P-wave annihilations may be almost equal [2].

Events for which P-wave annihilation occurred can be selected by requiring an L X-ray in coincidence. This will make it possible to measure the branching ratios to different final states from initial S- and P-states. Significant differences in the frequency of S- and P-wave annihilations to a given final state would indicate that the annihilation dynamics are dependant on the quantum numbers of the initial $\bar{p}p$ state. There is also the possibility (provided the splitting between the 1^3S_1 and 1^1S_0 states is large enough to differentiate them by the energies of the X-rays) that the spin, parity and charge conjugation quantum numbers of the initial state would be uniquely determined. At present the annihilation dynamics are not at all well understood; the measurement of such dependance on the initial angular momentum state would imply that any model of $\bar{p}p$ annihilation dynamics must predict these branching ratios from different initial angular momentum states.

2.3 Bound States and Exotic Resonances

The theory of quantum chromodynamics (QCD) has had considerable success in describing the properties of hadrons and their interactions. The quantum numbers of all hadrons and hadronic resonances so far observed

are consistent with the predictions of the quark model. This model predicts (or at least does not rule out) many other bound states which have as yet to be observed. As well as the familiar three-quark (qqq) and quark-antiquark ($q\bar{q}$) hadrons (baryons and mesons, respectively), there is not any theoretical reason why four-quark ($qq\bar{q}\bar{q}$) and six-quark ($qqq\bar{q}\bar{q}\bar{q}$) bound states should *not* exist. One of the reasons that they have not as yet been observed (if indeed they do exist) is that they may be very broad resonances, and therefore difficult to extract from the data. But if some of these states have high angular momentum the centrifugal barrier may give them longer lives, and hence cause them to be narrower and more easily identifiable [10]. The angular momentum of an atomic $\bar{p}p$ system is expected to change by one unit upon transition to a baryonium ($qq\bar{q}\bar{q}$) state [13]. The ability to detect an L X-ray, indicating P-wave annihilation, would aid in the search for narrow D-wave baryonium states. Previously such searches had only been conducted using liquid targets, so their ability to detect such high angular momentum baryonium states would have been hindered for reasons already discussed.

Perhaps of even greater fundamental interest are the so-called “glueballs”, bound states of two or more gluons (gg , ggg , etc.). These objects *must* exist if the theory of QCD has any validity. This is because the gluons, which are the intermediate bosons that carry the strong (or “color”) force are themselves “colored” objects, and so can interact strongly with each other. It is this feature of QCD which gives it many of its peculiar (as compared with quantum electrodynamics, or QED) and even astonishing predictions, such as the permanent confinement of quarks inside hadrons. Some of these resonances, and other exotic systems such as $q\bar{q}g$, are predicted to have narrow widths, with many of them lying below the $2m_p$ mass spectrum [1].

Chapter 3

The ASTERIX Detector

3.1 Overview

The ASTERIX detector, shown schematically in Figure 3.1, was designed to take full advantage of the high flux of low-energy antiprotons available at LEAR. The major considerations behind its design were to be able to study the $\bar{p}p$ X-ray spectrum and annihilation processes, with the capability of distinguishing (through X-ray detection) the initial angular momentum state of the $\bar{p}p$ system.

ANTIPROTON STOP EXPERIMENT WITH TRIGGER ON INITIAL X-RAYS (ASTERIX) AT LEAR

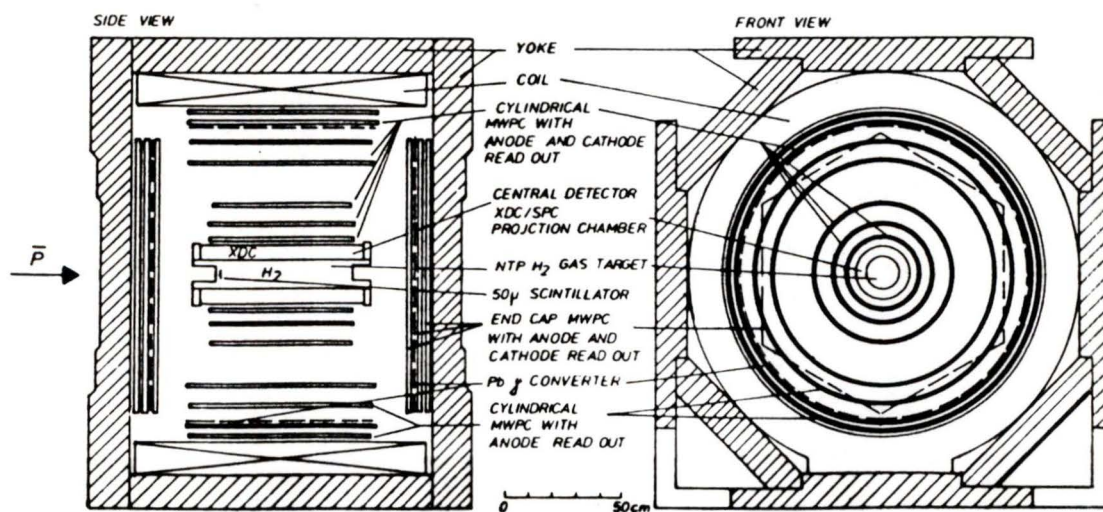


Figure 3.1: Schematic diagram of ASTERIX Detector (side and front views)

A previous experiment [6] involving some of the members of the AS-

TERIX collaboration had studied protonium X-rays with a four-atmosphere gaseous hydrogen target at the CERN proton synchrotron facility. At that time, that is, before the advent of the LEAR facility, the antiproton beam was of vastly inferior quality in several respects compared with what is available at LEAR. The intensity of antiprotons was several orders of magnitude less, the momentum spread was much greater and there was significant contamination of the beam by π^- 's. Thus, the pressure of the gas target had to be quite high to obtain a usable \bar{p} stop rate. Under these conditions, $\bar{p}p$ L X-rays were observed in $\approx 5\%$ of the \bar{p} stops. The high pressure of the target also served to suppress K X-rays, for reasons already cited.

The ASTERIX detector is an improvement on this experiment in several important ways:

- The target is maintained at a pressure of one atmosphere. The lower pressure greatly diminishes the collision-induced phenomena in the cascade process, allowing a much greater rate of radiative transitions of $\bar{p}p$ atoms to low n states, and so giving an improved yield of both L and K X-rays.
- The X-ray detector has high solid angle coverage (90% of 4π) and good detection efficiency and energy resolution in its active range (1 to 15 KeV).
- There is a charged-particle spectrometer which allows the complete reconstruction of events with several charged prongs and one neutral prong. This allows a detailed study of many of the final states and intermediate state resonances.
- The triggering system allows the selection of events by observing an X-ray from the $\bar{p}p$ cascade, or by charged prong multiplicities in the magnetic spectrometer or by the detection of γ -rays. This allows the efficient collection of data for many of the large number of possible decay channels.

The detection volume of the ASTERIX detector is a cylinder with length 1.6 m and internal diameter 1.8 m. There is an axial magnetic field of up to .82 Tesla. The beam line enters the target through a telescope-and-veto scintillator system. The target is surrounded by a cylindrical X-ray drift chamber (XDC). Surrounding the XDC are seven cylindrical multiwire proportional chambers used for charged-particle identification. There is a lead foil inserted between the fifth and sixth chambers for γ -ray detection. At the ends of the cylinder are two position-sensitive gamma detectors (PSGD). There is a solid angle coverage of 90% of 4π for the XDC, 50% for the magnetic spectrometer and 75% for the detection of γ -rays.

3.2 Target and XDC

The target and XDC assembly are shown in Figure 3.2. As mentioned

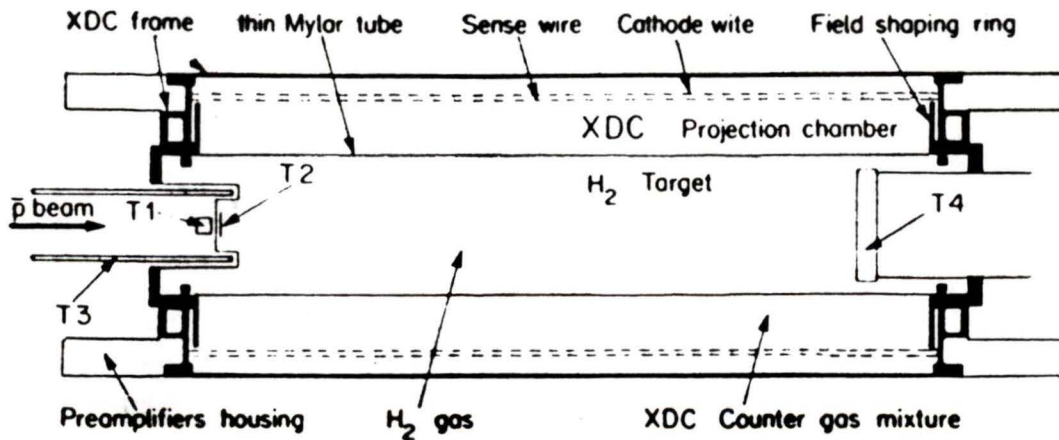


Figure 3.2: Side view of target and XDC assembly

in the preceding section, the antiproton beam enters the target through a telescope-and-veto scintillator arrangement. The incoming antiprotons first fire scintillator T_1 , which is also used as a moderator; its thickness can be varied to optimize the \bar{p} stop rate for a given beam momentum. A thin ($50\mu\text{m}$) scintillator T_2 is at the entrance to the target, surrounded by T_3 , a cylindrical scintillator. T_4 is positioned at the downstream end of

the target. A \bar{p} stop is defined by the firing of T_1 and T_2 and no signal from T_3 and T_4 ($T_1 T_2 \overline{T_3 T_4}$). This combination of signals will be the trigger to start the XDC drift-time measurements, which will be discussed in the next paragraph. T_3 is a veto for antiprotons which stop in T_2 : there is a very high probability that charged decay products from such a stop will trigger T_3 . T_4 is used to veto those antiprotons whose range exceeds the length of the target. The target has a length of 76 cm, a diameter of 16 cm, and contains H_2 at one atmosphere (NTP). This pressure was chosen to reduce the pressure-dependent cascade processes mentioned previously, and at the same time to allow the use of a thin ($6\mu\text{m}$) aluminized mylar foil to separate the target gas from the XDC gas. This thin foil is advantageous for two reasons:

- It is transparent to X-rays with energy greater than 1 KeV.
- It has a minimal effect on the charged particles traversing it, so the momentum resolution of the magnetic spectrometer is unaffected.

The foil also acts as the cathode plane for the XDC.

The XDC (see Figures 3.3 and 3.4) is a 50% argon–50% methane cylindrical drift chamber with a radial drift electric field. The central cathode, which separates the XDC from the target, is 90 cm long and 16 cm in diameter. There are 90 sets of alternating cathode wires and resistive ($R = 1500\Omega$) sense wires at a radius of 28.8 cm and 180 external cathode wires at 30 cm. This configuration creates 90 identical cells with drift lines along radii, or along identical spirals when an axial magnetic field is present. The operational principle of the XDC is to measure the drift time (measured from the \bar{p} stop trigger signal) of the ionization cluster created when an X-ray is absorbed by the counter gas. Because the mean free path of the X-rays is extremely sensitive to their energy, the drift time (in combination with the total charge collected) provides a reasonably accurate measurement of the energy ($\Delta E = 1.5 \text{ keV}$ at 9.0 keV [9]).

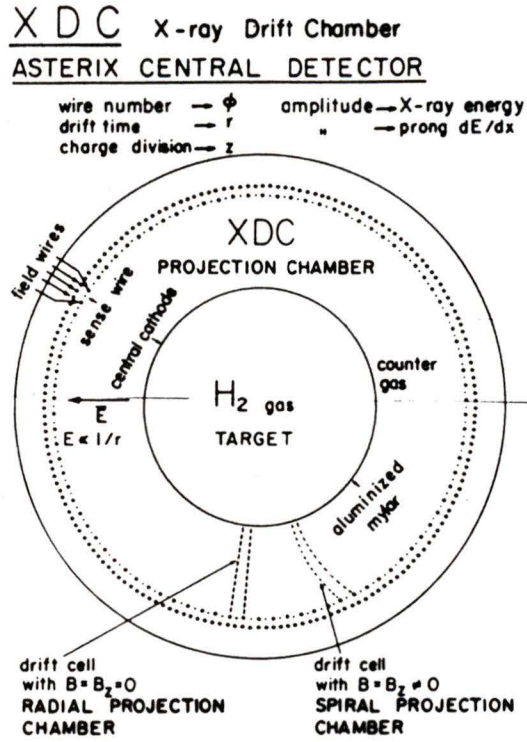


Figure 3.3: Schematic diagram of XDC (end view)

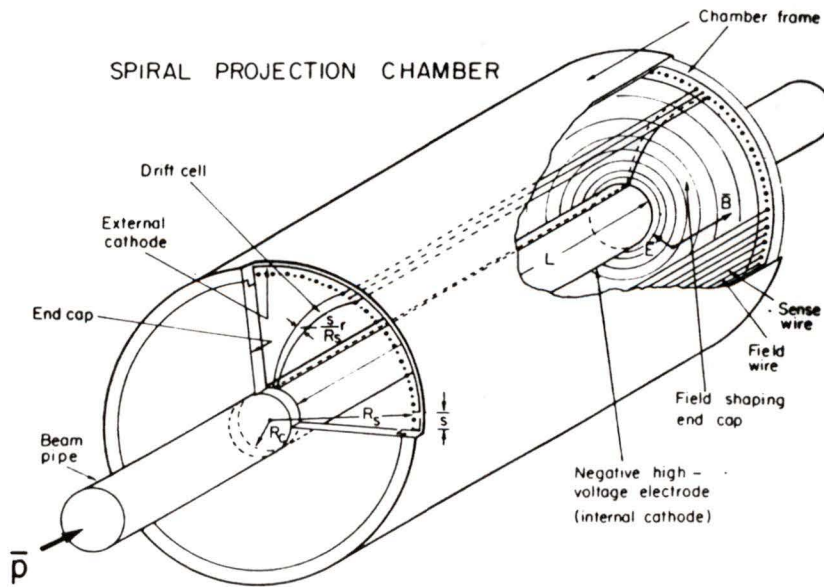


Figure 3.4: Schematic diagram of XDC (oblique view)

X-rays are distinguished from charged particles by their distinctive pulse shape: the pulses from X-rays are almost always spatially isolated clusters, typically contained in a volume of less than 1 mm^3 , while charged particles create ionization all along their path through the gas. Thus, an X-ray will typically produce a sharp peak in one drift cell and no peaks in adjacent cells (Figure 3.5), while a charged particle will either cause several adjacent cells to have significant peaks (Figure 3.6), or else produce a large energy deposition in one or two cells over a prolonged time period (Figure 3.7).

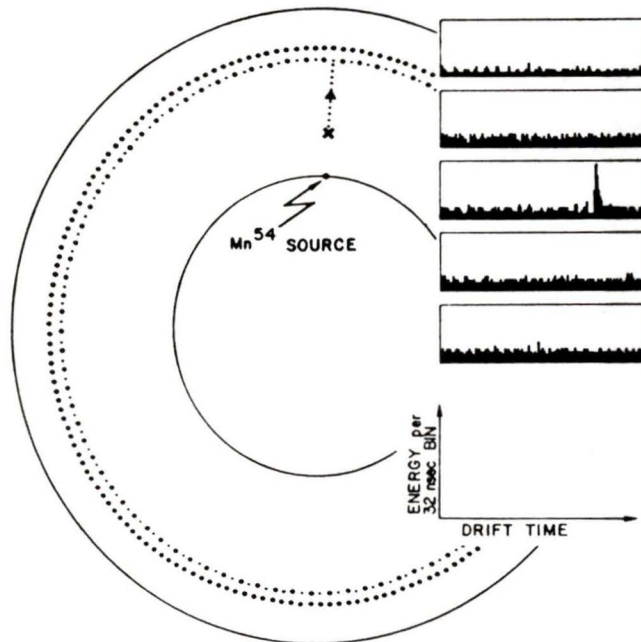


Figure 3.5: X-Ray event in XDC

The XDC is also capable of localizing the conversion point of the X-ray in the counter gas: the drift time provides the radius, the wire that fires determines the azimuthal angle and the z -coordinate is determined by charge-sensitive amplifiers located on both ends of each sense wire.

3.3 Magnetic Spectrometer

Charged-particle detection is performed by seven concentric cylindrical multi-wire proportional chambers (MWPC's) situated in an axial magnetic

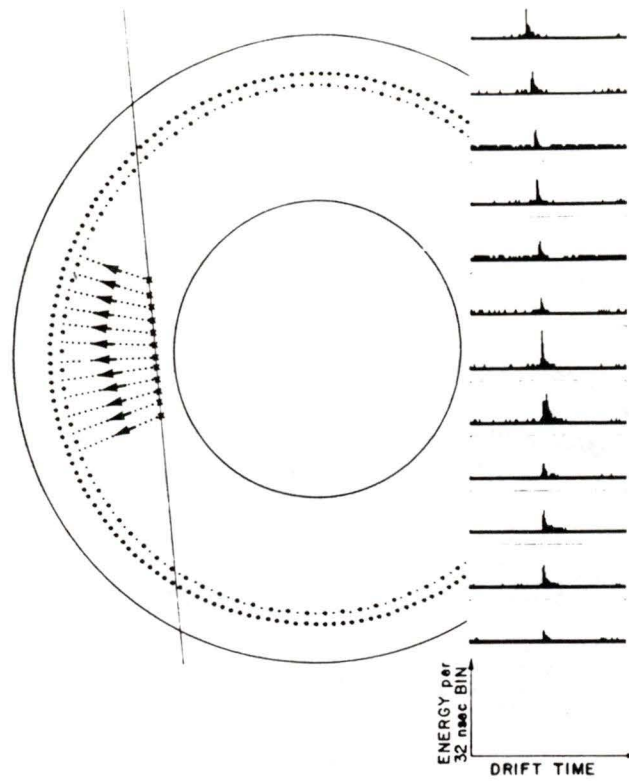


Figure 3.6: Cosmic ray traversing XDC

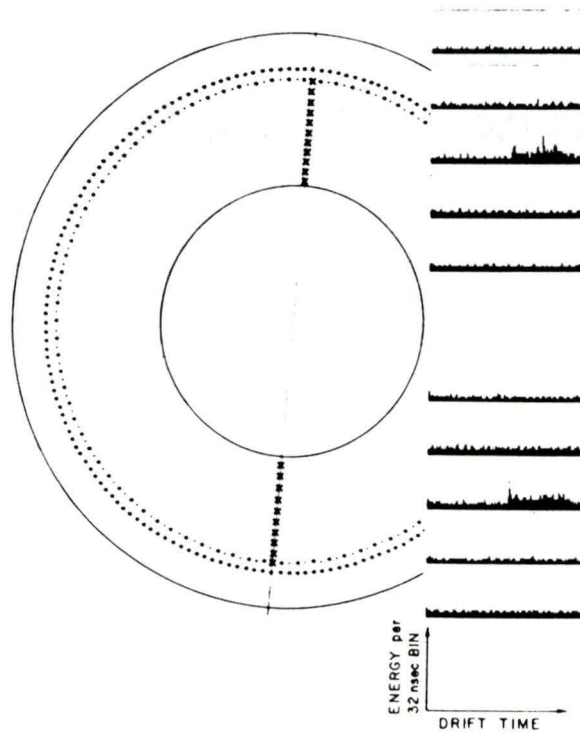


Figure 3.7: Cosmic ray traversing two opposite cells of XDC

field with strength up to .82 T. The chambers are designated, in order of increasing radius, C_1 , C_2 , Q_1 , Q_2 , P_1 , Q_3 and P_2 (see Figure 3.8). Five of

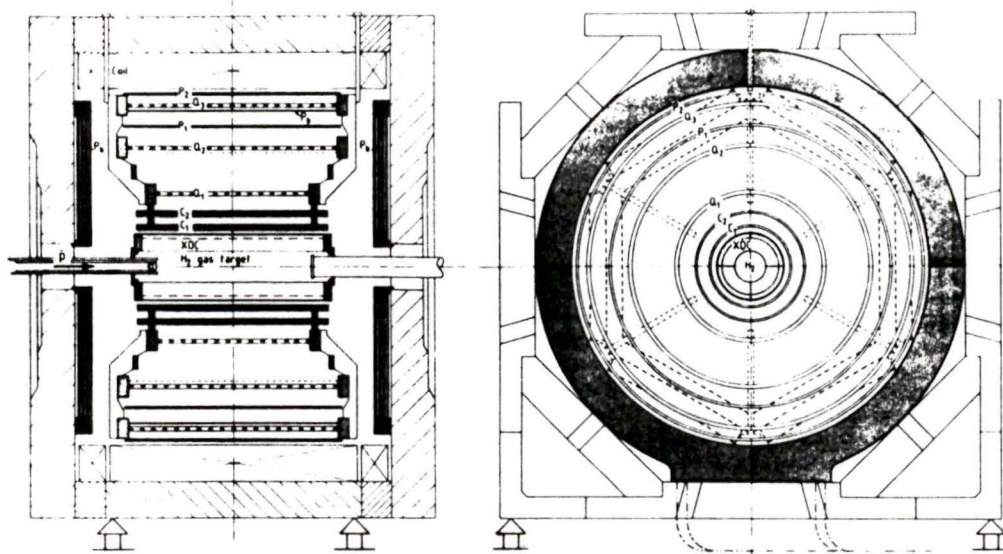
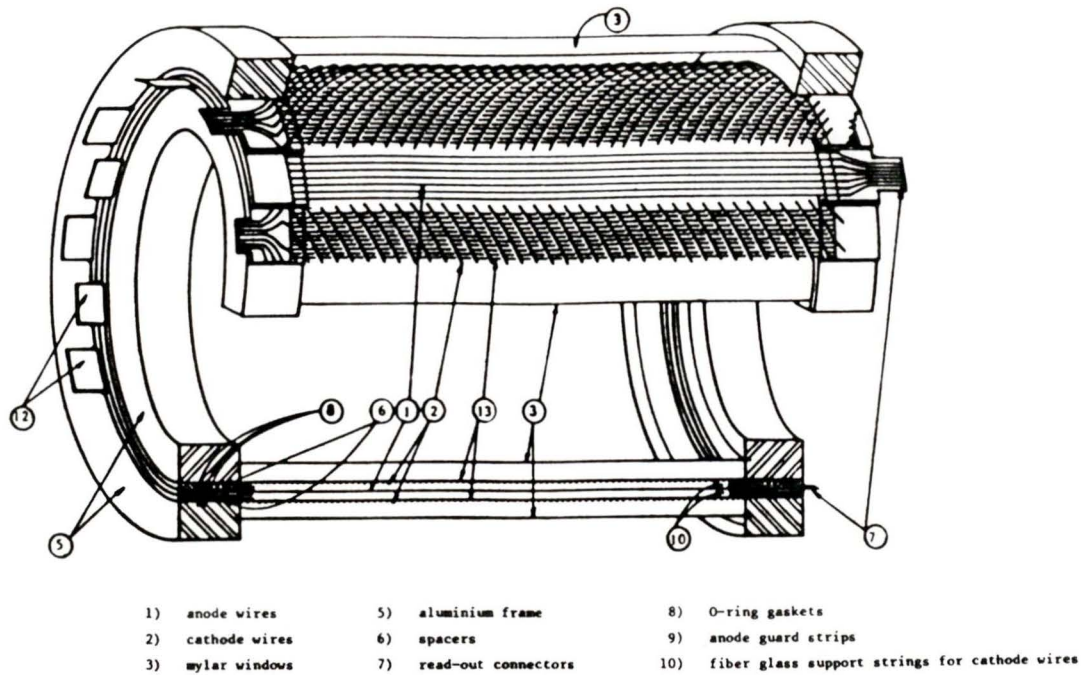


Figure 3.8: Positioning of MWPC's

the chambers (C_1 , C_2 , Q_1 , Q_2 and Q_3) have anode and cathode readout, thus giving r, ϕ and z position information, while the other two (P_1 and P_2) have anode readout only and so provide no z position information. All of the chambers are constructed with the anode wires stretched longitudinally, parallel to the cylinder axis. Those with cathode readout have either wires (Q_1 , Q_2 and Q_3) or 2 mm wide aluminized mylar strips (C_1 and C_2) wound helically around the cylinders. A cut-away view of the Q_1 chamber is shown in Figure 3.9. Details and dimensions of all the chambers are listed in Table 3.1.

The counter gas mixture used in all of the chambers is 68.4% argon, 28% isobutane, 3.4% methylal and .2% freon at a pressure of one atmosphere. The C-chambers have efficiencies greater than 98%, the Q-chambers 95% (anodes) and 85% (cathodes), while the P-chambers both have efficiencies very close to 100%. When combined with the solid-angle efficiency mentioned previously, the overall efficiency for the detection of charged particles

Figure 3.9: Cut-away view of Q_1 MWPC

	C_1	C_2	Q_1	Q_2	P_1	Q_3	P_2
Useful length	740	740	756	1040	960	1040	1070
Anode diameter	385.5	540.5	733.8	1188.8	1400	1610.8	1742
Cathode gap	6	6	6	6	6	6	6
Anode wire spacing	2.10	2.21	2.001	1.945	2.29	2.196	2.03
Cathode wire spacing	3.45	3.13	2.9	2.8	—	3.3	—
Anode wires	576	768	1152	1920	1920	2304	2688
Cathode wires/plane	288	384	576	960	—	1652	—
Cyl. proj. angle	35°	45°	46°44'	45°55'	—	49°23'	—
Operating voltage (kV)	3.4	3.4	4.3	4.3	3.0	4.3	3.0

Table 3.1: Characteristics of cylindrical MWPC's (dimensions in mm)

is of the order of 50%, if a “hit” is required in all seven chambers. The spatial resolution allows the determination of the event vertex to $\approx \pm 2$ mm in the x , y and z directions. The momentum resolution is expressed by

$$\Delta p/p \approx 2.5\% \times (p/500),$$

where p is the magnitude of the transverse component of the momentum, given in MeV/c. This will be discussed in more detail in the next chapter.

3.4 γ -ray Detection

The detection of γ -rays is handled by two systems which, although distinct, operate under the same principles. They are able to provide positional information only; no energy measurements are possible. A .9 radiation length cylindrical lead converter, inserted between chambers P_1 and Q_3 covers the barrel region while two endcaps, each consisting of three MWPC's with a .9 radiation length lead converter placed between the first and second chambers, covers the forward and backward regions. The cylindrical lead γ converter can be seen in Figures 3.1 and 3.8, and the endcap detector layout is shown in Figure 3.10.

A high-energy γ , converting into an electron-positron pair in the lead, will fire the two chambers behind the lead; thus a γ will be defined by hits in the two detectors behind the lead and no hit in the chamber in front of the lead. The solid angle coverage is 25% for the endcaps and 50% for the cylinder for a total of 75%. The conversion probability for both the endcap and cylinder γ detectors is $\approx 40\%$ ¹. Combined, these two factors give an overall π^0 detection efficiency of $\approx 10\%$. The spatial resolution is ± 5 mm for the cylindrical detector and ± 2 mm for the endcaps. Details and dimensions of the endcap detectors are summarized in Table 3.2.

¹For 100 MeV γ -rays.

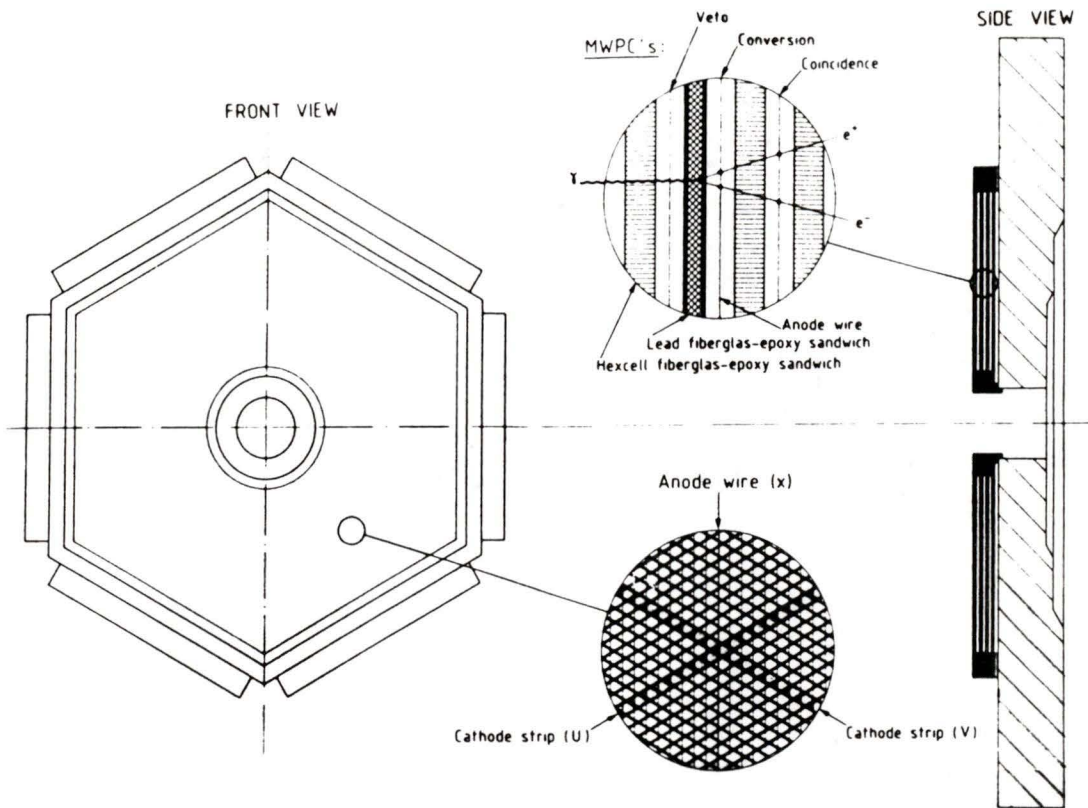


Figure 3.10: Endcap PSGD configuration

Anode-cathode gap	5 mm
Anode wire spacing	4 mm
Cathode strip spacing	4 mm
Cathode-Anode angle	$\pm 60^\circ$
Number of anode wires	320
Number of cathode strips	2×320
Sensitive area	1.3 m^2

Table 3.2: Characteristics of Endcap γ Detectors

3.5 Tracking

In order to be analysed, an event must be first detected, and then recognised as such. This seems obvious, but these two steps are quite distinct. The former depends on the physical detector itself, i.e. the particles must leave a trace of their passage through the detector by interacting with it in some way; so whether or not a charged particle will be detected depends on such things as the composition and pressure of the gas mixture in the proportional counters, the voltages on the sense wires and so on. The latter depends on how the various interactions between the particle and the detector are interpreted; it is essentially a problem of pattern-recognition for which the analysis is almost always performed on a computer, following the rules of an often very complicated algorithm. There is no guarantee that an event, once detected, will be correctly recognized. Thus, the overall efficiency of the detection system is actually the product of the physical efficiency of the detector itself and the efficiency of the pattern-recognition (or “tracking”) programme.

The first step in the data analysis procedure is to identify X-rays, charged particles and γ -rays from the raw data.

The method of identification for X-rays from the XDC data was discussed in Section 3.2. Once an X-ray has been identified as such, its total energy is obtained from the total charge collected, and its conversion co-ordinates in the XDC are obtained from drift-time measurements (r), charge division on the anode wires (z) and drift-cell number (ϕ).

For charged particles the programme relies on positional information only². The actual tracking only identifies a track and calculates the momentum and charge of the particle that produced it; it does not identify what type of particle produced the track. Track recognition is not a trivial

²This is not strictly true; the tracking procedure can use the XDC information, which uses drift time measurements, to get the co-ordinates of two extra “hits”, in addition to those from the MWPC’s.

problem, particularly if there are a large number of charged tracks, or if it involves a K_s^0 , whose lifetime ($\approx 10^{-10}$ s) is such that they decay before completely traversing the detector, creating a “sub-vertex” for the event. For each charged particle the programme must determine which points belong to that particular track and then fit the points to a helix. The radius of the helix is proportional to the momentum in the plane transverse to the magnetic field (x - y plane), while the pitch of the helix gives the longitudinal or z momentum. The charges of the particles are determined by the direction of curvature in the magnetic field, while the vertex is determined from where the calculated tracks intersect. Obviously, at least two tracks are needed to determine the event vertex. The direction of the charged particles immediately after the annihilation is extrapolated from orientation of the reconstructed tracks at the vertex. The errors in the determination of the magnitude and direction of the momentum of each charged particle are calculated based on the assumed spatial resolution of the chambers and the χ^2 (“goodness of fit”) for each track. A reliable determination of these errors depends on several factors:

- The spatial resolution of the detectors must be well known.
- The geometry of the detector must be well known, i.e. the true spatial position of all the sense wires must be precisely determined. Even very small misalignments or deformities of the different chambers can lead to significant reductions in resolution and tracking efficiencies. This will be discussed further in relation to the data analysis.
- It is desirable that the magnetic field is known accurately throughout the sensitive volume of the detector, including any possible anomalies.

The detection and identification of γ -rays was described in Section 3.4.

Chapter 4

Analysis of $\pi^+\pi^-\pi^0$ Events

4.1 Significance

The $\pi^+\pi^-\pi^0$ decay channel is of interest for several reasons. It can be reached from six different initial states of the $\bar{p}p$ system, it has several possible intermediate resonant states and the overall rate for $\bar{p}p \Rightarrow \pi^+\pi^-\pi^0$ is quite high, $(6.9 \pm .4)\%$ [14]. A thorough analysis of this channel could provide useful information in a number of different areas:

- If combined with the capability for detecting X-rays, this channel could give another measure of the relative rates of annihilations from S- and P-state.
- Because the intermediate resonances are dependent on the angular momentum and isospin quantum numbers of the initial $\bar{p}p$ state, a thorough analysis of the amplitudes of these intermediate states can provide an even more detailed picture of the branching ratios from the different initial states and give some idea of the dependency of the annihilation dynamics on these quantum numbers.
- This channel is useful in determining the performance of almost all aspects of the ASTERIX detection and data analysis systems: in order for any of the physics results of the experiment to be reliable it

is necessary that the operational characteristics, including efficiencies and resolutions, be well known and understood.

4.2 Aims of Analysis

The major aims of this analysis were to utilize the conversion co-ordinates of γ -rays from π^0 decay for the kinematical fitting of events with a $\pi^+\pi^-\pi^0$ final state, and to see if this technique would provide a cleaner and more definitive $\pi^+\pi^-\pi^0$ signal than had been previously observed. Other attempts to analyze this channel [14,15] used only the the charged-particle tracks (1-constraint or "1C" fit). This "1C" method of analysis is unable to reduce the contamination of the data sample by non- $\pi^+\pi^-\pi^0$ events below $\approx 14\%$. For a detailed analysis of the different initial states contributing to the $\pi^+\pi^-\pi^0$ final state it is essential that the background either be reduced to negligible levels or that it be known very precisely. But the background (due mainly to events whose final state is $\pi^+\pi^-(n\pi^0)$, where $n \geq 2$) is not at all well known, in part because of the lack of knowledge of the relative amplitudes of the intermediate resonances possible in the channels that contribute to the contamination. So it would be preferable to try to reduce the background level as much as possible by applying very stringent (compared with the 1C fit) criteria to the selection of $\pi^+\pi^-\pi^0$ events. The γ -ray positional information enables the three-constraint (3C) fitting procedure to subject the $\pi^+\pi^-\pi^0$ candidates to a more rigorous selection system, and so reject a much higher proportion of non- $\pi^+\pi^-\pi^0$ events.

4.3 Tracking of $\pi^+\pi^-\pi^0$ Events

The tracking programme fits the points produced by a charged pion to a circle in the plane transverse to the magnetic field and to a line in the z - φ plane, where φ is the azimuthal angle about the axis of the helix. The

radius of curvature (ρ), center of curvature in the x - y plane (x_c, y_c) and the constants α and β from the straight line fit $z = \alpha\varphi + \beta$ are calculated for both the charged pions (independently) by the fitting routine, and are then used to calculate the perpendicular and longitudinal components of the momentum and the event vertex. The directions of the particles in the transverse plane are determined by the directions of the calculated circles at the point where they intersect (the event vertex).

The fitting routine also calculates the error matrices for each track, for both the circle and straight line fits. These contain the variances and covariances of the calculated fit parameters:

$$\mathbf{E}_{trans} = \begin{bmatrix} \sigma_\rho^2 & \sigma_{\rho x}^2 & \sigma_{\rho y}^2 \\ \sigma_{\rho x}^2 & \sigma_x^2 & \sigma_{xy}^2 \\ \sigma_{\rho y}^2 & \sigma_{xy}^2 & \sigma_y^2 \end{bmatrix}, \mathbf{E}_{long} = \begin{bmatrix} \sigma_\alpha^2 & \sigma_{\alpha\beta}^2 \\ \sigma_{\alpha\beta}^2 & \sigma_\beta^2 \end{bmatrix}$$

These quantities are dependent on the spatial resolution of the wire chambers and on how well the points fit the calculated tracks.

An important implication of the finite spatial resolution is that the error in the determination of the radius of curvature (σ_ρ) increases in direct proportion to ρ itself. It follows from this that the error in the momentum determination also increases directly with increasing ρ , so the overall momentum resolution of the detector gets worse with increasing momentum. This will be discussed in more detail in relation to the results of the 3C fitting.

The γ -ray conversion co-ordinates are much easier to determine, as it is basically just a matter of drawing a line between the hit wires and the calculated vertex and then calculating where it crosses the lead converter. The spatial resolutions of the γ detectors are set at constant values: $\sigma_{Q_3} = \pm 0.5$ cm for the cylindrical converter and $\sigma_{PSGD} = \pm 0.2$ cm for the endcap detectors. Obviously, the z conversion co-ordinate is fixed for the endcap detectors.

4.4 Kinematic Fitting

The tracking programme finds the momenta of the charged particles, the event vertex and the γ conversion co-ordinates; it makes no “judgments” about *what* the charged particles were, or whether the γ -rays originated from a single π^0 . The kinematic fitting programme determines what type of event has occurred by setting up a hypothesis (in this case, that the event was $\bar{p}p \Rightarrow \pi^+\pi^-\pi^0$), and then determining the probability that a given event is consistent with the hypothesis. Omitting the mathematical details for now, the procedure can be described as follows. Given the quantities determined by the tracking programme (along with their errors), and supposing that the particles are indeed $\pi^+\pi^-\pi^0$, how much adjustment of these parameters is required to make them consistent with the hypothesis? The more adjustment that is needed, the less likely it is that the given event is actually of the type given in the hypothesis. The amount of adjustment needed (normalized over the errors in the original determination of the parameters) is called the “ χ^2 ” value for the fit.

In actual fact, it is not the parameters calculated in the tracking programme that are used in the kinematic fitting; a transformation of variables is performed. In this new definition the event vertex is taken as the origin. The new variables are:

$$\begin{aligned} H &\equiv 1/p_{\perp} \\ \theta &\equiv \tan^{-1} \frac{p_z}{p_{\perp}} \\ \phi &\equiv \tan^{-1} \frac{p_y}{p_x} \end{aligned}$$

where $p_{\perp} = \sqrt{p_x^2 + p_y^2}$. The inverse of the perpendicular momentum is used because its distribution is approximately Gaussian [16], whereas the distribution of the momentum itself is not.

The errors corresponding to the new variables are given by [17]¹

$$\sigma_\theta^2 = \frac{1}{(1 + \tan^2 \theta)^2} \left(\frac{\sigma_\alpha^2}{\rho^2} + \frac{\sigma_\rho^2}{\rho^2} \tan^2 \theta \right) \quad (4.1)$$

$$\sigma_\phi^2 = \frac{1}{(1 + \tan^2 \phi)^2} \left(\frac{y'^2}{x'^4} \sigma_x^2 + \frac{\sigma_y^2}{x'^2} - 2y' \frac{\sigma_{xy}^2}{x'^3} \right) \quad (4.2)$$

$$\sigma_H^2 = \frac{\sigma_\rho^2}{\rho^2} H^2 \quad (4.3)$$

$$\sigma_{H\phi}^2 = \frac{1}{\rho^2(1 + \tan^2 \phi)} \left(\frac{y'}{x'^2} \sigma_{x\rho}^2 - \frac{\sigma_{y\rho}^2}{x'} \right) \quad (4.4)$$

$$\sigma_\theta^2 = \frac{\sigma_\gamma^2}{z'^2} \quad (4.5)$$

$$\sigma_\phi^2 = \frac{\sigma_\gamma^2}{x'^2 + y'^2} \quad (4.6)$$

for the charged particles (4.1-4.4) and γ -rays (4.5-4.6), respectively, where:

$$x' \equiv x_{vertex} - x_c$$

$$y' \equiv y_{vertex} - y_c$$

$$z' \equiv z_{vertex} - z_c$$

The actual spatial resolutions for the γ detectors are taken to be constants:

$$\sigma_\gamma^2 = .5 \text{ cm}(\text{cylinder})$$

$$\sigma_\gamma^2 = .2 \text{ cm}(\text{endcaps})$$

¹S ome of the expressions given in [17] contained errors which were corrected in the computer code.

The covariance matrix for the ten measured variables is

$$\mathbf{G} = \begin{bmatrix} \sigma_{\theta\pi_1}^2 & 0 & 0 & 0 & 0 & 0 & 0 & 0 & 0 & 0 \\ 0 & \sigma_{\phi\pi_1}^2 & \sigma_{H\phi\pi_1}^2 & 0 & 0 & 0 & 0 & 0 & 0 & 0 \\ 0 & \sigma_{H\phi\pi_1}^2 & \sigma_{H\pi_1}^2 & 0 & 0 & 0 & 0 & 0 & 0 & 0 \\ 0 & 0 & 0 & \sigma_{\theta\pi_2}^2 & 0 & 0 & 0 & 0 & 0 & 0 \\ 0 & 0 & 0 & 0 & \sigma_{\phi\pi_2}^2 & \sigma_{H\phi\pi_2}^2 & 0 & 0 & 0 & 0 \\ 0 & 0 & 0 & 0 & \sigma_{H\phi\pi_2}^2 & \sigma_{H\pi_2}^2 & 0 & 0 & 0 & 0 \\ 0 & 0 & 0 & 0 & 0 & 0 & \sigma_{\theta\gamma_1}^2 & 0 & 0 & 0 \\ 0 & 0 & 0 & 0 & 0 & 0 & 0 & \sigma_{\phi\gamma_1}^2 & 0 & 0 \\ 0 & 0 & 0 & 0 & 0 & 0 & 0 & 0 & \sigma_{\theta\gamma_2}^2 & 0 \\ 0 & 0 & 0 & 0 & 0 & 0 & 0 & 0 & 0 & \sigma_{\phi\gamma_1}^2 \end{bmatrix} \quad (4.7)$$

To formulate more precisely the fitting technique, we wish to determine the vector \mathbf{c} (the correction to \mathbf{m} , the vector of the measured variables) which minimizes the scalar quantity

$$\chi^2 = \mathbf{c}^T \mathbf{G}^{-1} \mathbf{c} \quad (4.8)$$

while simultaneously fulfilling the constraint equations

$$\mathbf{f}(\mathbf{m} + \mathbf{c}) = 0 \quad (4.9)$$

where the superscript T signifies the transpose of a vector or matrix. There are ten measured variables (θ , ϕ and H for each of the charged pions; θ and ϕ for each of the photons) and five equations of constraint: $\Sigma \vec{p} = 0$ (three equations); $\Sigma E = 2m_p$; $(M_{inv})_{\gamma\gamma} = m_{\pi^0}$. Because the constraint equations are not linear in the variables used, it is necessary to linearize them by expanding them in a Taylor series about an approximate value $\bar{\mathbf{c}}$ (initially set to zero):

$$\mathbf{f}(\mathbf{m} + \mathbf{c}) = \mathbf{f}(\mathbf{m} + \bar{\mathbf{c}}) + \mathbf{B}[\mathbf{c} - \bar{\mathbf{c}}] + \dots \quad (4.10)$$

where \mathbf{B} is the derivative matrix defined by

$$B_{\lambda i} \equiv \frac{\partial f_\lambda}{\partial c_i} \quad (4.11)$$

If we now define

$$\mathbf{r} \equiv \mathbf{f}(\mathbf{m} + \bar{\mathbf{c}}) - \mathbf{B}\bar{\mathbf{c}}$$

we can rewrite the constraint equations as

$$\mathbf{f}(\mathbf{m} + \mathbf{c}) = \mathbf{B}\mathbf{c} + \mathbf{r} = 0 \quad (4.12)$$

Equations 4.8 and 4.9 are combined into one equation, and the method of Lagrangian multipliers [18] is used in an iterative manner to find the correction vector c which will minimize χ^2 :

$$\chi^2 = \mathbf{c}^T \mathbf{G}^{-1} \mathbf{c} + 2\alpha \mathbf{f} \quad (4.13)$$

Taking partial derivatives with respect to c_i ($i = 1, 2, \dots, 10$) and α_λ ($\lambda = 1, 2, \dots, 5$, the number of constraints) and setting them to zero, we are left with a system of fifteen equations in fifteen unknowns which are then solved by matrix inversion. The steps are repeated with the new values c_i until the value of the constraints are reduced to a specific value. If this value is not reached after ten iterations the event is discarded. It is defined as

$$S \equiv \left| \left(\sum_{i=1}^4 p_{xi} + p_{yi} + p_{zi} + E_i \right) + (M_{inv}^2)_{\gamma\gamma} - 2m_p - m_{\pi^0}^2 \right| \quad (4.14)$$

The question of what value of χ^2 to choose as the ‘‘cutoff’’ for good and bad events depends on the nature of the available information. Theoretically, if the statistical distributions of the measured quantities are known, one can choose the confidence interval that one works at by looking up the value in table, which depends only on the number of degrees of freedom in the fit. The number of degrees of freedom is simply the difference between the number of constraint equations (in this case 5) and the number of unmeasured quantities (in this case 2), so we are left with 3 degrees of freedom (hence a 3C fit). In contrast, the 1C fit has the same number of constraint equations, but the three components of momenta and the mass

of the undetected particle (assumed to be a π^0) are unknown. In general, the fewer constraints, the more restrictive (i.e. lower) the χ^2 cut has to be in order to obtain the same confidence level.

It must be understood that the interpretation of the χ^2 test in terms of confidence levels, that is in terms of what percentage of events will have χ^2 values less than or equal to the cutoff values, applies only to true events: it will tell us what proportion of actual events that will be rejected by the test, but not how many false events will be accepted. The rejection of real events, again assuming that the errors are estimated correctly, is essentially a question of mathematics, independent of the physics. The (mistaken) acceptance of false events, on the other hand, depends on the nature of competing processes which can mimic the one in which we are interested. We could therefore assume that the performance of the 1C fit could be made identical to that of the 3C fit in the case of the rejection of real events by simply adjusting the χ^2 cutoff value. Thus, the motivation for using the 3C fit must lie in the fact that it can reject a higher proportion of false events for a given confidence level than the 1C fit. The reasons for this will be made clear in the following chapter.

4.5 Data Set Criteria

The data used were taken in October 1985 at a beam momentum of 100 MeV/c. The total data set consisted of two subsets according to the trigger logic that selected them. One set ($\approx 2 \times 10^6$ events) had the trigger condition call for two charged prongs in the first four wire chambers, while the other trigger condition ($\approx 8 \times 10^5$ events) required as well a “one gap” condition in the XDC. This meant that there must be an X-ray candidate defined by the criteria mentioned in section 3.2. These trigger conditions will be referred to from here on by their ASTERIX runcode designations, 3421 and 21421, respectively. The fulfillment of the trigger conditions did

not imply that the tracking programme would recognize two tracks in the first case or two tracks and one X-ray in the second case; the criteria used for this fast selection were much looser than those of the tracking programme. The major reason for using these triggers was to collect a large number of a given type of event in an efficient manner, rather than having to cull through millions of events to find those that were appropriate for a given analysis. This produced raw data tapes (RDTs) with a very high proportion of two-prong events.

The RDTs were then processed by the tracking programme which produced data summary tapes (DSTs). These tapes were subsequently used for the analysis, although they were further condensed by producing second-level DSTs with only those events that had two γ -rays in addition to two valid charged-particle tracks as defined by the tracking programme. Statistics for the cuts applied to the data by the fitting programme were recorded as well for all of the two-prong events, regardless of the number of photons detected. These cuts will be described in detail below.

Before attempting a kinematical fit, an event was required to pass the following set of "track-quality" cuts:

1. The event record must be accepted as valid, i.e. there must be no anomalies in the record format.
2. There must be exactly 1 vertex.
3. That vertex must be within the fiducial volume, i.e. the vertex coordinates must satisfy $|z_{vertex}| \leq 35$ cm and $|r_{vertex}| \leq 7$ cm.
4. There must be exactly 2 charged prongs.
5. The charged prongs must have opposite helicities.
6. There must be 7 points defining each charged prong².

²There are 9 possible points per track: 7 from the magnetic spectrometer and two from the XDC.

In addition, the value of the missing mass squared of the $\pi^+\pi^-$ pair had to lie within a given range: $|(M_{missing}^2)_{\pi^+\pi^-}| \leq .5 \text{ GeV}^2/c^4$. And, of course, there were required to be exactly two γ 's detected in order to fit them to the π^0 .

Only events that passed *all* of these tests were submitted to the kinematical fitting routine.

It should be noted that events submitted to the fitting routine were required to pass one additional cut before the actual fitting began. This was that the initial estimate of the angle between the plane defined by the event vertex and the two γ conversion positions, and the missing momentum vector ($\vec{p}_{missing}$), had to be less than 7° .

Events submitted to the fitting routine were accepted or rejected on the basis of the χ^2 value for the fit, provided that the event was fit in ten iterations or less. The value of the total χ^2 for a "good event" was set at $\chi^2 \leq 10$, although results were also taken for cutoff values of $\chi^2 \leq 30$ and $\chi^2 \leq 100$ for comparative purposes. The events were also divided on the basis of whether or not an X-ray was detected. The results and their significance will be described in the following chapter.

Chapter 5

Results of Analysis

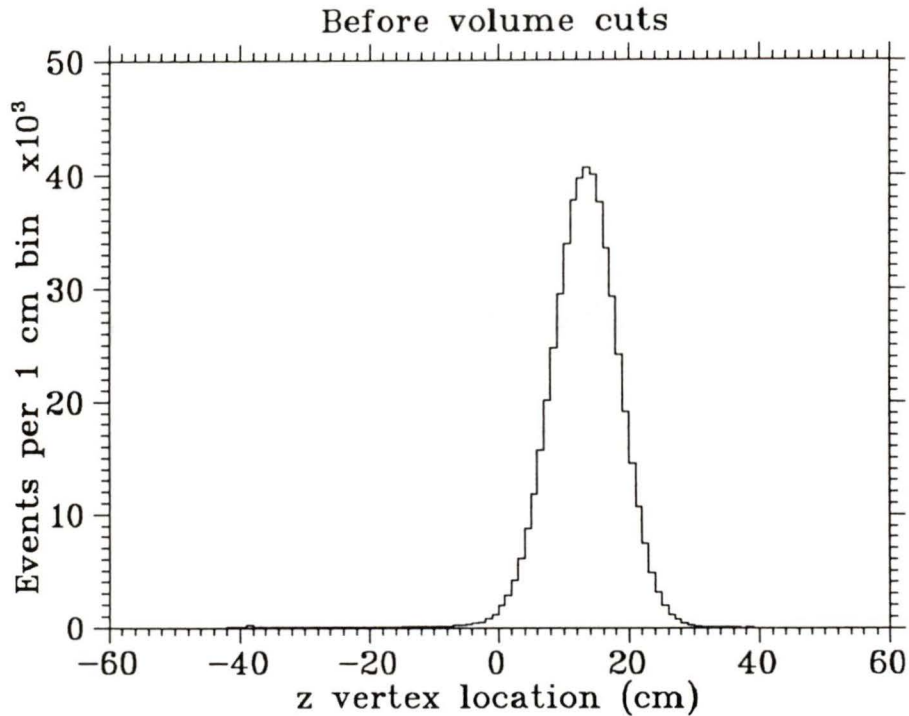
5.1 Effects of Cuts Prior to Fitting

The cuts described in the previous chapter served to eliminate many events from the original data set. All of these cuts, their purposes and effects, will be described below.

The first restriction is that the event must have only one vertex. As the vertex position is calculated by finding where the charged-particle tracks cross, there should be a uniquely determined vertex for a 2-prong event. If there are less than two tracks, there will be no vertex. If there are two or more tracks, the tracks must pass within a certain specified distance of each other for there to be a vertex. For a two prong event, failing this cut would usually imply that the track fitting is very poor, or possibly that the tracks actually came from separate vertices.

The event vertex must be contained in the fiducial volume of the target. This eliminates events in which the \bar{p} is captured by the counter gas, the endcaps or some other part of the detector. It would also eliminate events in which a γ converted somewhere outside of the target. At a momentum of 100 MeV/c almost the entire beam stops within the z -region of the detector (see Figure 5.1), but there are a non-negligible number of stops outside the radius of the target.

There must be two charged-particle tracks. The fast trigger used to se-

Figure 5.1: \bar{p} z stopping distribution

lect events does not necessarily guarantee that the tracking programme will find two tracks; this cut eliminates events which the fast trigger selects but which do not meet the more stringent criteria of the tracking programme.

The tracks must have opposite helicities, i.e. the charged particles must have opposite charges. This cut requires no further explanation.

There must be at least seven points defining each charged-particle track. There is a strong correlation between the momentum resolution and the number of points on a track. There are nine possible points (two from the XDC and seven from the proportional chambers), but two of these have no z -position information. Thus this cut implies that there will be at least five z -points for fitting the longitudinal momentum and at least seven for the transverse momentum.

The raw missing mass squared¹ of the $\pi^+\pi^-$ ($(M_{missing}^2)_{\pi^+\pi^-}$) must be in the range of $-.5$ to $.5$ GeV^2/c^4 . This cut is made largely to save time; there is very little probability of any event outside this region, whether real or false, being successfully fitted. The histogram of the raw $(M_{missing}^2)_{\pi^+\pi^-}$ of the fit events (Figure 5.3) confirms this.

Statistics for the efficiency of these cuts are shown in Table 5.1.

Cut Description	Runcode		Total
	3421	21421	
Accepted as valid event	2045503	793793	2839206
Exactly one vertex	1662539	701611	2364150
Vertex in fiducial volume	1599830	680945	2280775
Exactly two tracks	1491145	546642	2037797
Opposite charges	1461884	544461	2006345
Seven points/track	943349	478778	1422127
Exactly two γ 's	170610	160503	331113
$(M_{missing}^2)_{\pi^+\pi^-} \leq .5 \text{ GeV}^2/c^4$			79266

Table 5.1: Statistics for October 1985 2-Prong Data

5.2 $(M_{missing}^2)_{\pi^+\pi^-}$ Plots

The raw $(M_{missing}^2)_{\pi^+\pi^-}$ distribution for the fitted events is an important indicator of how well the fitting procedure is performing in selecting $\pi^+\pi^-\pi^0$ events and eliminating background. If we had a detector with perfect spatial resolution, we would expect this plot to be a delta function located at the π^0 mass. The finite spatial (i.e. momentum) resolution of the ASTERIX

¹If n particles are detected, then the missing mass squared is defined as:

$$M_{missing}^2 \equiv (E_{total} - \sum_{i=1}^n E_i)^2 - |\vec{p}_{total} - \sum_{i=1}^n \vec{p}_i|^2$$

It is equivalent to the invariant mass of any missing particle(s).

detector smears this delta function into a Gaussian-like distribution, whose width is a measure of the detector's charged-particle resolution. The fact that the peak extends beyond the missing-mass thresholds for $2\pi^0$ and $3\pi^0$ events indicates that the fitted distribution is subject to possible contamination from these types of events. But the mere fact that the distribution extends beyond the threshold for contamination events does not necessarily imply that there is actually significant contamination; it could be that the fitting routine is able to distinguish between real and false $\pi^+\pi^-\pi^0$ events in this crucial region. Thus, it is necessary to determine the amount of contamination in the distribution of fit events.

It is necessary first of all to determine what the shape of the curve would be if there were no contamination: what would we expect to see if we had a sample which we knew contained *only* real π^0 events? One must make some assumptions (based, of course, on what we believe to be the characteristics of our detector resolution) as to the shape of the $(M_{missing}^2)_{\pi^+\pi^-}$ distribution. As explained in the previous chapter, the resolution function of the magnetic spectrometer is approximately Gaussian in $1/p$. This results in a $(M_{missing}^2)_{\pi^+\pi^-}$ distribution that is almost Gaussian, and quite symmetrical about the π^0 mass².

The simplest method of estimating the amount of contamination is to fold the experimental distribution about the π^0 mass and measure the skewness. This method assumes that all of the events on the low side of the π^0 mass are real events. This is a reasonable assumption because the π^0 has the smallest mass of any single particle that can be produced along with the $\pi^+\pi^-$ pair; i.e. there are no sources of background events with invariant mass less than m_{π^0} . This technique can be used with both the 1C and 3C fits. This gave sensible results in the previous 1C analyses [14,15], in which there were definite "shoulders" of contamination on the

²This was determined by a Monte Carlo simulation of $\pi^+\pi^-\pi^0$ events in which the charged pion momenta were "smeared" in this manner.

high side of the distributions (see Figure 5.2). But it was found that the

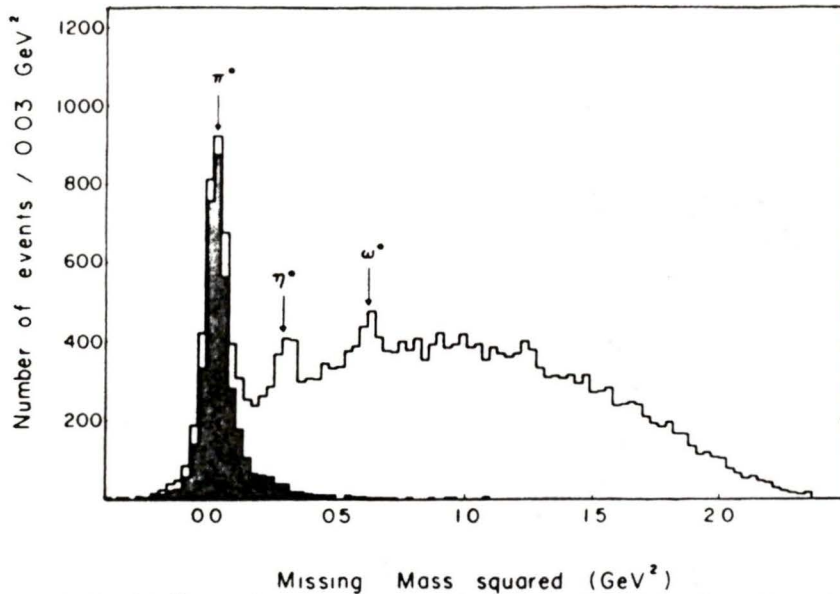


Figure 5.2: $(M_{missing}^2)_{\pi^+\pi^-}$ distribution from bubble chamber data

$(M_{missing}^2)_{\pi^+\pi^-}$ distribution for the 3C fit had no such “shoulder”; indeed, there were slightly *fewer* events on the high side than on the low side of the π^0 mass.

Another method (which can be used only with the 1C fit) is to simulate $2\pi^0$ events by selecting $\pi^+\pi^-$ pairs at random from a set of $\pi^+\pi^-\pi^+\pi^-$ events and seeing what fraction of them can be fitted successfully. This could be somewhat unreliable because of the different rates of formation of $\rho^0(770)$ and $f^0(1270)$ resonances for the 2-prong and 4-prong final states [14].

Because there seemed to be no obvious method to determine the amount of contamination in the fitted data set, a Monte Carlo simulation was done in order to try to explain the shape.

5.3 Monte Carlo Simulations

It was obvious immediately that the true momentum resolution was worse than the value estimated in the ASTERIX proposal: with the resolution set

to the value given in the proposal, the resulting $(M_{\text{missing}}^2)_{\pi^+\pi^-}$ distribution was much narrower than the actual one. Based on the assumption that all (or nearly all) of the fitted ($\chi^2 \leq 10$) events were real π^0 events, it was found that the best fit to the experimental distribution was when the momentum resolution was taken to be 3.2% at 500 MeV/c. Figure 5.3 shows the $(M_{\text{missing}}^2)_{\pi^+\pi^-}$ distribution for the fit ($\chi^2 \leq 10$) events with the Monte Carlo distribution overlaid (smooth curve).

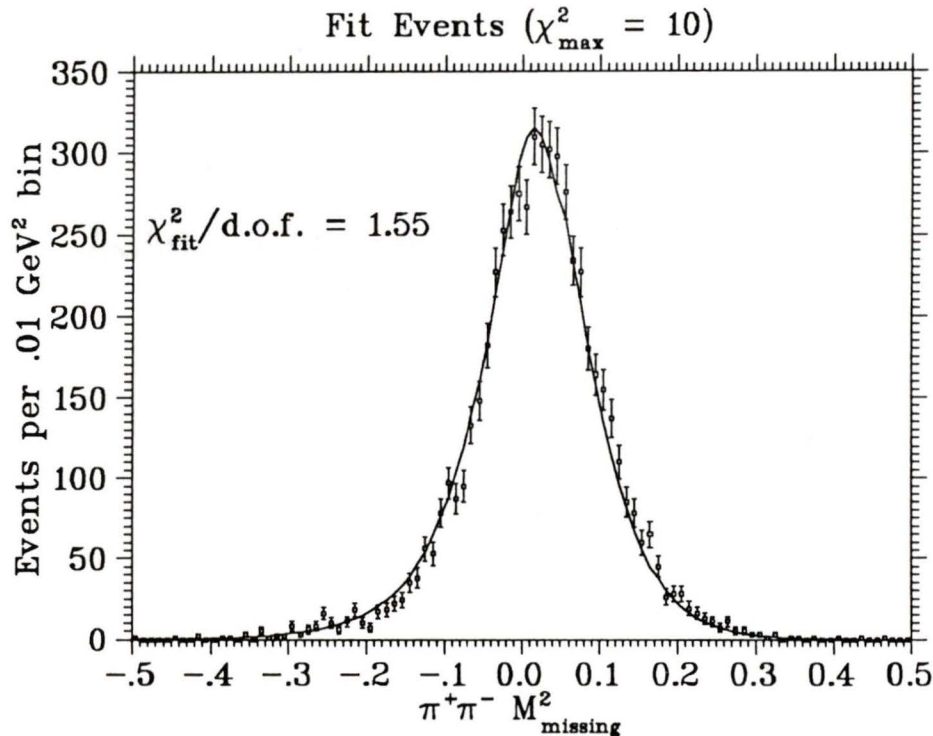


Figure 5.3: $(M_{\text{missing}}^2)_{\pi^+\pi^-}$ distribution and Monte Carlo approximation for fit events ($\chi^2 \leq 10$)

The fit to the experimental distribution was done over the largest continuous range for which there were no bins without any events. Although the Monte Carlo programme was quite simplified, in that it did not take into account the detector geometry, the fit to the data was quite remarkable. In particular, it reproduced the slight excess of events on the low side of the π^0 mass. Using the same resolution function, Monte Carlo distribu-

tions of $(M_{\text{missing}}^2)_{\pi^+\pi^-}$ were produced for $2\pi^0$, $3\pi^0$, η and ω events. These were fit to the raw $(M_{\text{missing}}^2)_{\pi^+\pi^-}$ distribution of the total data set for the range $-.5$ to $.5$ GeV^2/c^4 (Figure 5.4). Again, a very good fit was obtained, further suggesting that the momentum resolution used in the Monte Carlo calculations was at least close to the actual resolution of the ASTERIX detector.

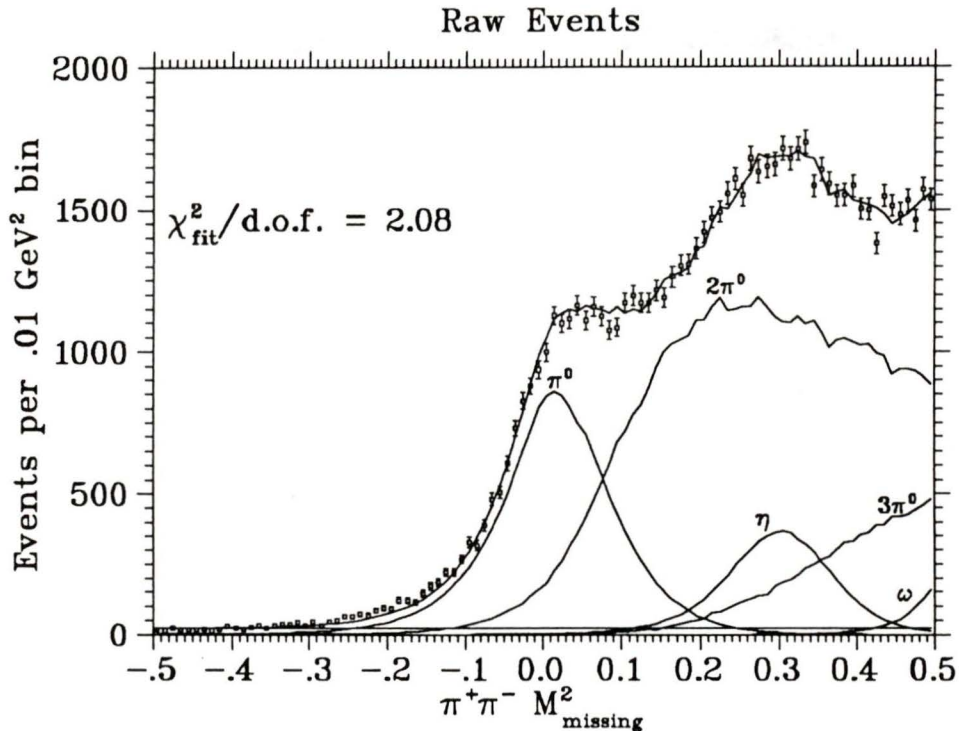


Figure 5.4: $(M_{\text{missing}}^2)_{\pi^+\pi^-}$ distribution and Monte Carlo approximation for complete data set

The best fit to the $(M_{\text{missing}}^2)_{\pi^+\pi^-}$ distribution for the fit events was obtained with a very small component of $2\pi^0$ contamination ($\approx .5\%$ of the π^0 component), although the χ^2 was only a slight amount lower than for a pure π^0 distribution. So on the basis of the $(M_{\text{missing}}^2)_{\pi^+\pi^-}$ plots it would appear that the 3-constraint fit was almost completely successful in eliminating contamination. It is evident, however, that many of the real $\pi^+\pi^-\pi^0$ events were also eliminated, since the π^0 component of the total

data set has three times as many events as the fit spectrum.

Fits were also attempted for the $(M_{missing}^2)_{\pi^+\pi^-}$ distributions that had cutoff values of χ^2 of 30 and 100 (Figures 5.5 and 5.6, respectively). Neither of these distributions could be fit well (compared with the total data set and the χ^2 10 data set) with any of the combinations of π^0 and the various contamination components. But this can actually be seen as further evi-

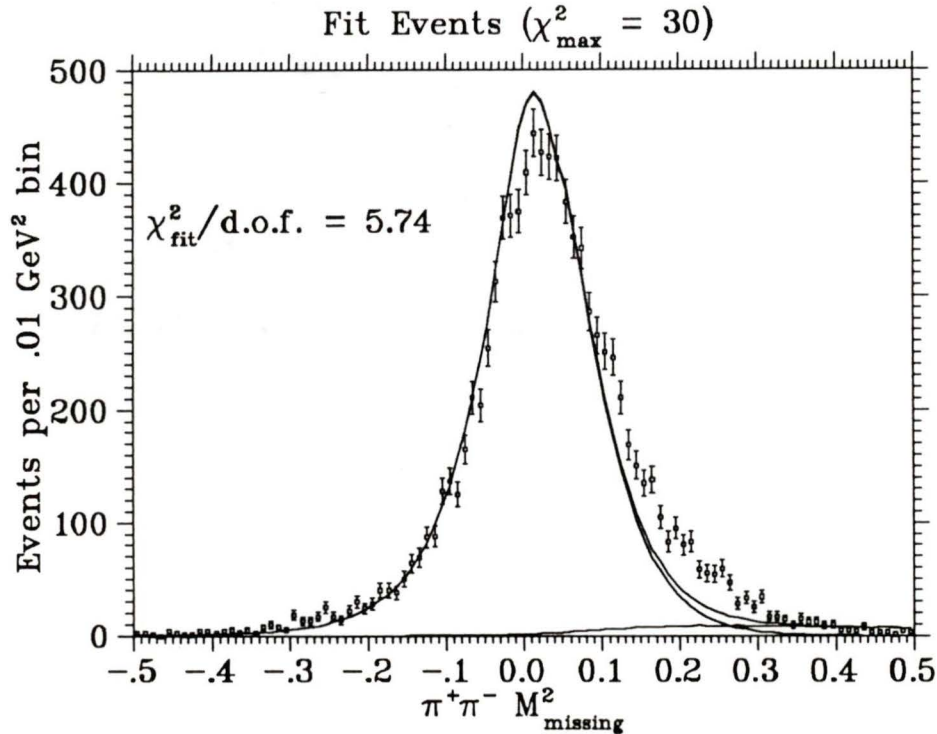


Figure 5.5: $(M_{missing}^2)_{\pi^+\pi^-}$ distribution and Monte Carlo approximation for fit events ($\chi^2 \leq 30$)

dence of the effectiveness of the 3C fit: the fitting routine does not eliminate contamination uniformly, i.e. the magnitudes of the contamination components are not reduced by constant amounts over their respective ranges. In general, the contamination components are reduced preferentially at high values of $(M_{missing}^2)_{\pi^+\pi^-}$. So it is only in the total spectrum, where the contamination distributions are unbiased, and in the fit spectrum, where we have a virtually pure sample of π^0 events, that a good fit can be obtained

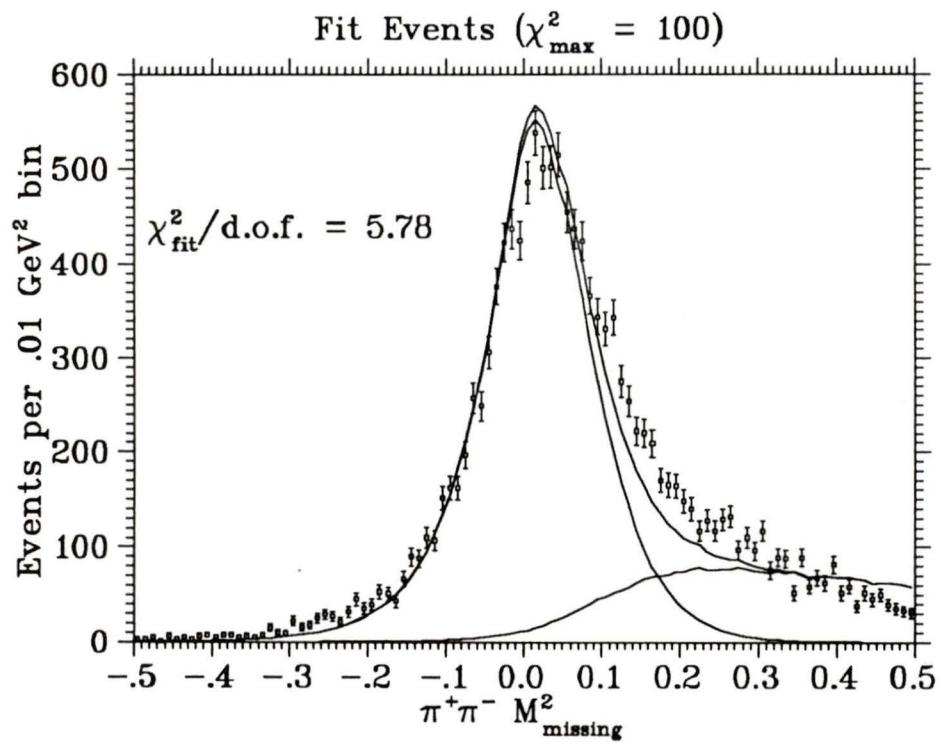


Figure 5.6: $(M^2_{\text{missing}})_{\pi^+\pi^-}$ distribution and Monte Carlo approximation for fit events ($\chi^2 \leq 100$)

with the Monte Carlo distributions.

Figure 5.7 shows the distribution of χ^2 values for the fit events. The χ^2

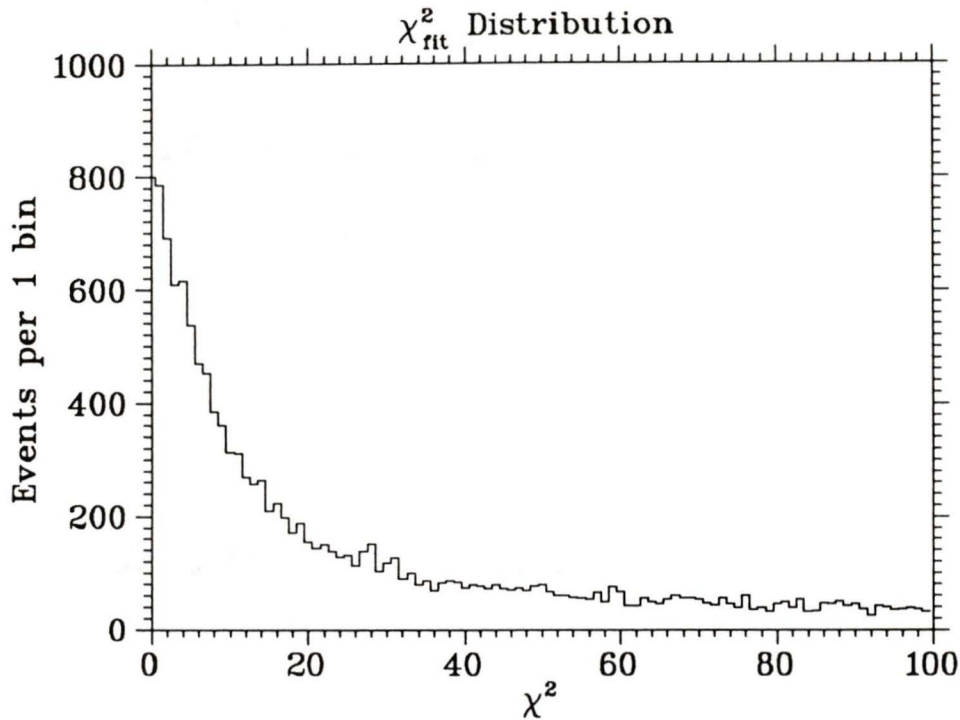


Figure 5.7: χ^2 distribution for fit events

value for the fit is related to the probability of finding real events with χ^2 values less than or equal to the cutoff value. A χ^2 of 10 for three degrees of freedom should mean $\approx 98\%$ of the real events should have a χ^2 value less than or equal to 10. But the fitting routine selected only $1/3$ ($\approx 33\%$) of the events. The present resolution of the detector is significantly worse than had been estimated; the χ^2 values of the fit are calculated on the basis of these wrong estimations. We can use the knowledge of what fraction of real events were fitted to estimate the “real” cutoff value of χ^2 ; that is, the value of χ^2 for which the probability of a real event being selected is $\approx 1/3$. This value turns out to be ≈ 1.6 , which for a three constraint fit is an extremely “tight” cut.

5.4 Why the 3C-Fit Works

There can be little doubt that the γ position information improves the fitting of $\pi^+\pi^-\pi^0$ events, from the point of view of background elimination. Indeed, when one compares the $(M_{missing}^2)_{\pi^+\pi^-}$ spectrum of the fitted events with that of the total data set (i.e. all those events that have two charged prongs and two γ -rays) it seems amazing that the π^0 peak can be extracted from amidst the almost overwhelming background. But an understanding of the kinematics of π^0 decay into two γ -rays shows quite clearly why the fitting programme is able to eliminate the background.

Because pions are much lighter than protons and antiprotons (≈ 140 MeV/c² versus ≈ 940 MeV/c²), they move off from the annihilation vertex with high momenta. The mean momentum of the π^0 's for the fit events was ≈ 570 MeV/c. In the center of mass of the π^0 the decay is isotropic and the γ -rays are back-to-back. But in the laboratory the γ -ray distribution is strongly peaked in the forward direction: the higher the momentum of the π^0 , the more probable it is that both γ -rays will be found within a small cone around the direction of the π^0 . For a given energy there is a minimum angle between the γ -rays, taken with respect to the event vertex. This angle corresponds to both γ -rays being emitted at 90° to the π^0 direction in its rest frame, and is given by

$$\theta_{min} = 2 \tan^{-1} \frac{1}{\beta\gamma}, \quad (5.1)$$

where

$$\gamma = \frac{E_{\pi^0}}{m_{\pi^0}}$$

$$\beta = \sqrt{1 - \frac{1}{\gamma^2}}$$

Because of the tendency for most of the events of a given energy to cluster

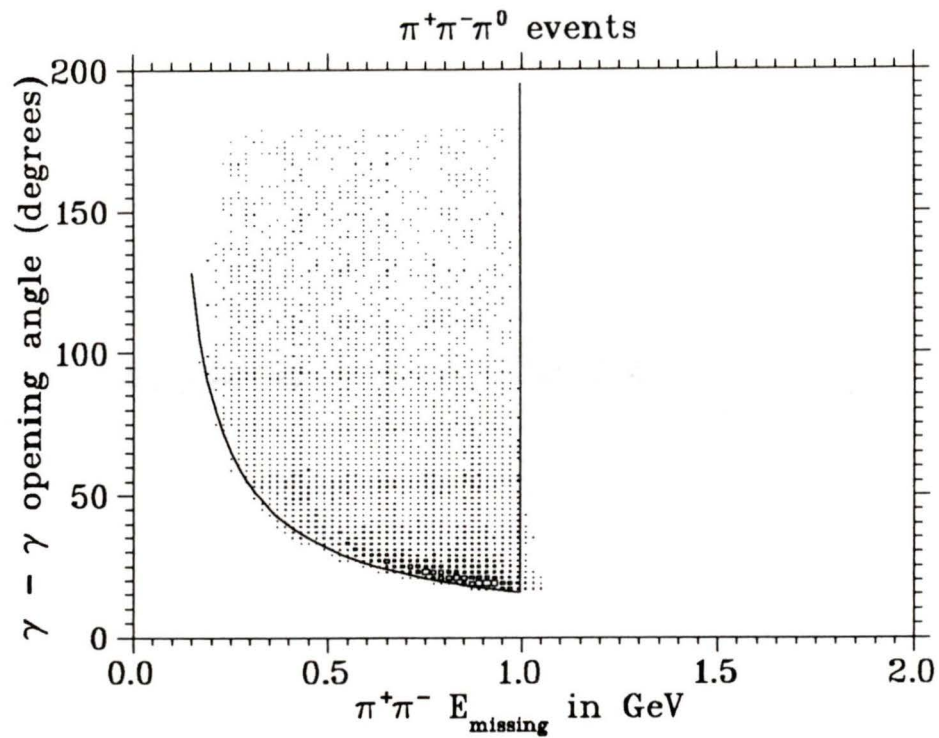
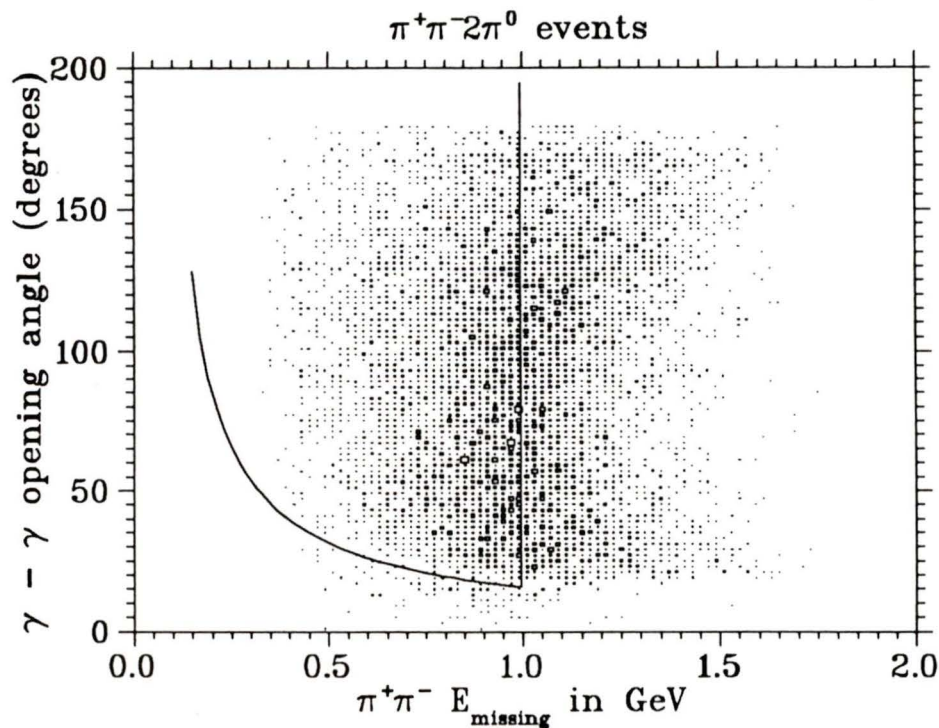
about this minimum value there is in many cases a severe restriction placed on the possible energy of the π^0 , and hence on the amount of correction that can be applied to the momenta of the charged pions³.

Monte Carlo calculations were performed (with the momentum resolution function mentioned previously) to determine the “overlap” of real π^0 events for which both γ -rays are detected (Figure 5.8), with $2\pi^0$ (Figure 5.9) and $3\pi^0$ (Figure 5.10) events. For the contamination events two γ -rays (out of four or six, respectively) were selected at random. The opening angles of the γ -rays were plotted as a function of the $\pi^+\pi^-$ missing energy (i.e. the energy of the hypothetical π^0) and the distributions compared.

It can be seen that the real events all lie within a well-defined region and tend to cluster near the minimum value for the given value of missing energy. The $2\pi^0$ and $3\pi^0$ events, on the other hand, are much more widely dispersed and do not show this tendency to cluster around the minimum value. The experimental plot agrees very well with the Monte Carlo plot for real π^0 events.

But even if a false event has an opening angle that is compatible with the missing energy, it is also necessary for the *direction* of the missing momentum to “agree” with the locations of the γ -rays. This means that two independent angles must be sufficiently close to particular values in order for the event to be fit with a low χ^2 . One of these angles is that between the plane of the two γ -rays and the missing momentum direction. Monte Carlo calculations show that this cut would eliminate $\approx 73\%$ of the $2\pi^0$ events and $\approx 85\%$ of the $3\pi^0$ events, while keeping $\approx 95\%$ of the real π^0 events. Although this is probably somewhat optimistic, there can be no doubt that this is a very efficient cut in the sense of a “signal-to-noise” ratio.

³It was found that the fitting routine primarily adjusted the charged-particle parameters, and made little correction to the γ positions. This was shown by observing the different contributions to the total χ^2 of the fit, and as well by observing negligible effects on the χ^2 distribution when the spatial resolution for γ -rays was artificially increased up to three times its nominal value.

Figure 5.8: Monte Carlo simulation of γ -rays from $\pi^+\pi^-\pi^0$ eventsFigure 5.9: Monte Carlo simulation of γ -rays from $\pi^+\pi^-2\pi^0$ events

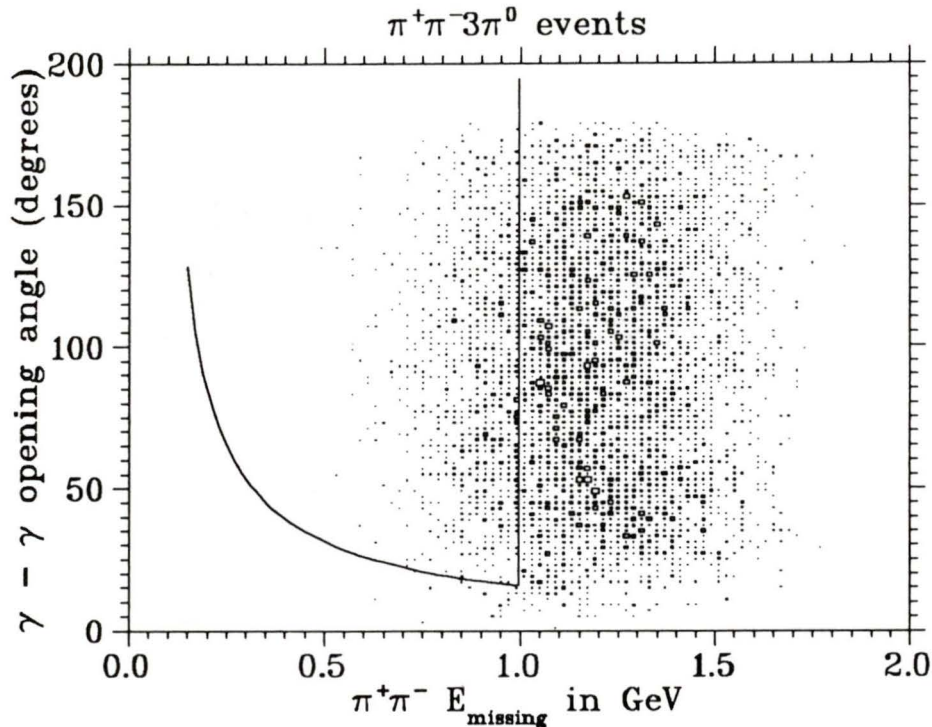


Figure 5.10: Monte Carlo simulation of γ -rays from $\pi^+\pi^-3\pi^0$ events

It is not certain whether this cut is actually necessary, that is, whether or not the χ^2 cut would eliminate the false events which do not pass this cut. The histogram of the cosine of this angle for the fit events seems to indicate that there are perhaps several hundred more good events outside the cutoff value, and there is no reason to believe that if the χ^2 cut can eliminate false events *within* the accepted range, it will not perform as well outside of this range. In any case, the cut on the angle serves to save a significant amount of computation in attempting to fit events that will ultimately be rejected.

The other angle to consider (even assuming that the above mentioned one is sufficiently close) is the relative angle (in the plane of the γ -rays) of the missing momentum with respect to the two photons. The momenta of the γ -rays are very sensitive to this angle, producing a relatively meagre chance of random γ -rays from multiple- π^0 events being aligned sufficiently close to enable fitting of the event with a small enough χ^2 .

All of these effects combined will mean that few, if any, of the multiple- π^0 events will make any kinematic sense at all when confronted with a restrictive cut on the χ^2 of the fit.

So having established the effectiveness and the reasons for the effectiveness of the 3-constraint kinematic fitting procedure, we can now move on to the fit events themselves and try to see what they can tell us about the performance of the ASTERIX detector, and more important, about the physics of $\bar{p}p \Rightarrow \pi^+\pi^-\pi^0$ reaction.

5.5 Detector Performance

In order to be able to obtain reliable physics results it is necessary that the performance characteristics of the detector are well understood. We need to know the efficiencies, useful ranges of operation and any possible malfunctions of each separate part of the detection system. Only then are we able to correct the data for the biases that are introduced by the detection system. For a sophisticated, multipurpose detector such as the one used in this experiment, the problem of determining how the detector might introduce biases is very complex. The only reasonable way to understand how the different parts of the detector perform as a whole is to construct a detailed Monte Carlo programme that incorporates all of the known properties of the detector: the geometry, the materials from which it is constructed; the characteristics of the gases; a detailed map of the magnetic field, and the stopping profile of the beam in the target. As well, any known malfunctions of the detector can be incorporated into the programme. Such a programme can reveal many subtle effects due to the detector which could be mistaken for actual properties of the data. Such an analysis is beyond the scope of this thesis; however, the data itself can reveal several of the grosser features of the detector's performance.

The vertex distribution shows that virtually all of the beam is stopped

within the z -range of the fiducial volume, but there is significant spread in the radial distribution. The centroid of the vertex distribution is located 13 cm downstream from the center of the target and has a full width at 1/2 maximum (FWHM) of 13 cm (see Figure 5.1).

The distribution of the initial value of the sum of the constraints S (defined in Equation 4.14) shows an interesting feature that is most likely due to some (as yet undetermined) malfunction of the detector. Figure 5.11 shows the distribution of $S_{initial}$ for the fit events. The curve is monotonically decreasing (allowing for statistical aberrations) except for a distinct small peak that starts abruptly at $S_{initial} = 1.6$. This smaller “sub-distribution”, which is more easily seen when the plot is expanded (Figure 5.12) is the same shape as the main one. An examination of the raw $(M_{missing}^2)_{\pi^+\pi^-}$ distribution for those events with $S_{initial} \geq 1.6$ shows that they are real $\pi^+\pi^-\pi^0$ events, as the distribution is definitely centered at the π^0 mass (Figure 5.13). The number of events ($\approx 3.5\%$ of the total set of fit events) would tend to indicate peculiar circumstances occurred in a particular run. Future work of this data should try to explain this feature by examining the anomalous events more closely.

One item that could be determined even without examining the data (but which is clearly visible upon examination of the Dalitz plots, which will be discussed in the next section), is that the range of momentum detection has a definite lower limit caused by the radius of curvature of the charged-particle trajectories in the magnetic field. Below a certain momentum (which from the fit data is ≈ 100 MeV/c) the radius of curvature is too small to allow the particle to traverse enough chambers such that there are seven points defining the track, as is demanded by the fitting routine.

Already discussed was the momentum resolution for charged particles, which turned out to be significantly worse than anticipated. This showed up clearly in the Monte Carlo fits to the missing-mass spectrum. To get

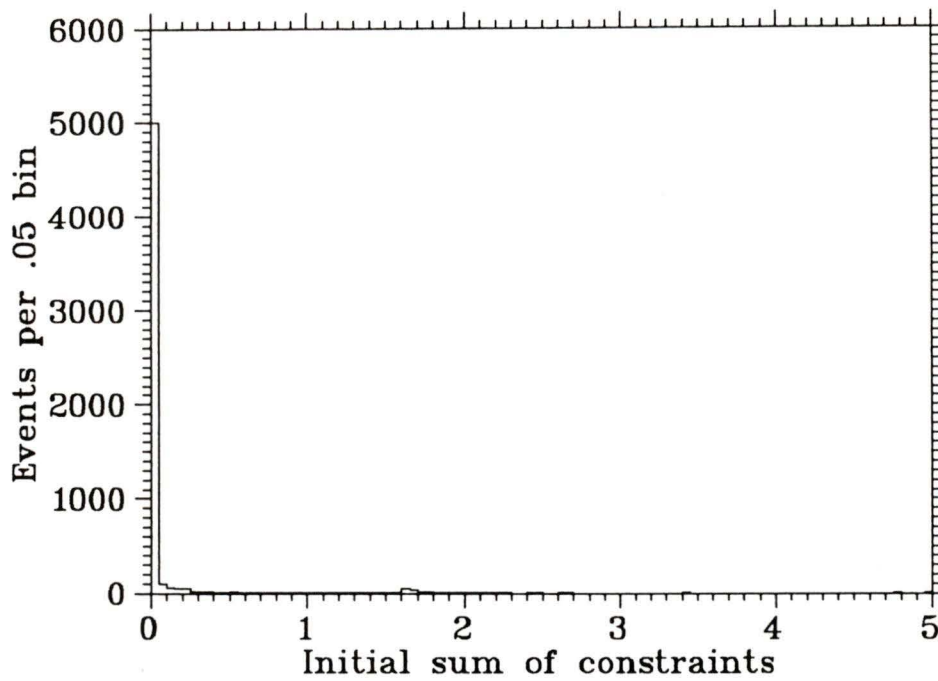


Figure 5.11: Initial value of sum of constraints

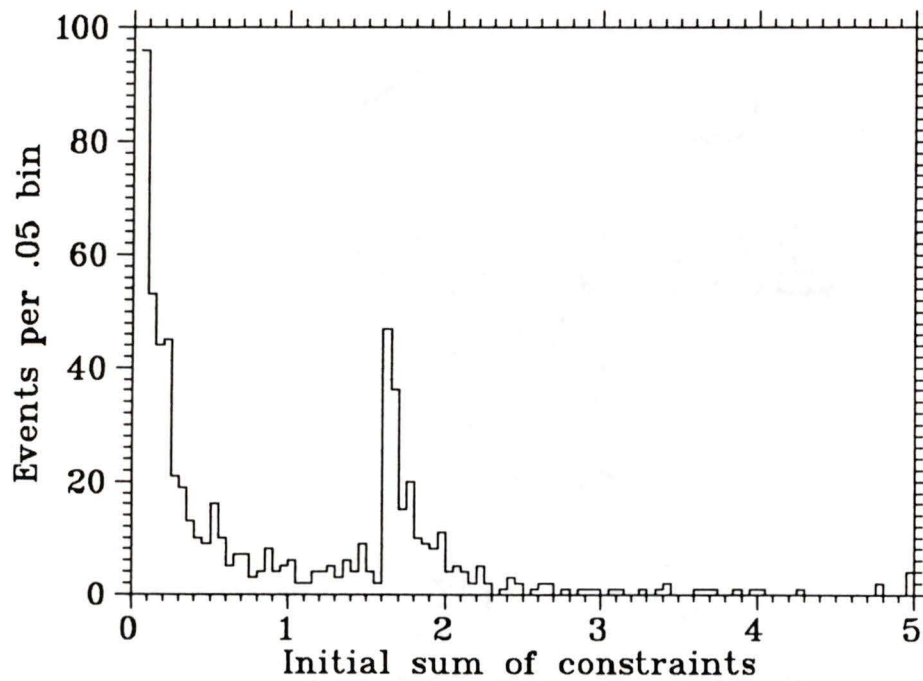


Figure 5.12: Initial value of sum of constraints (expanded)

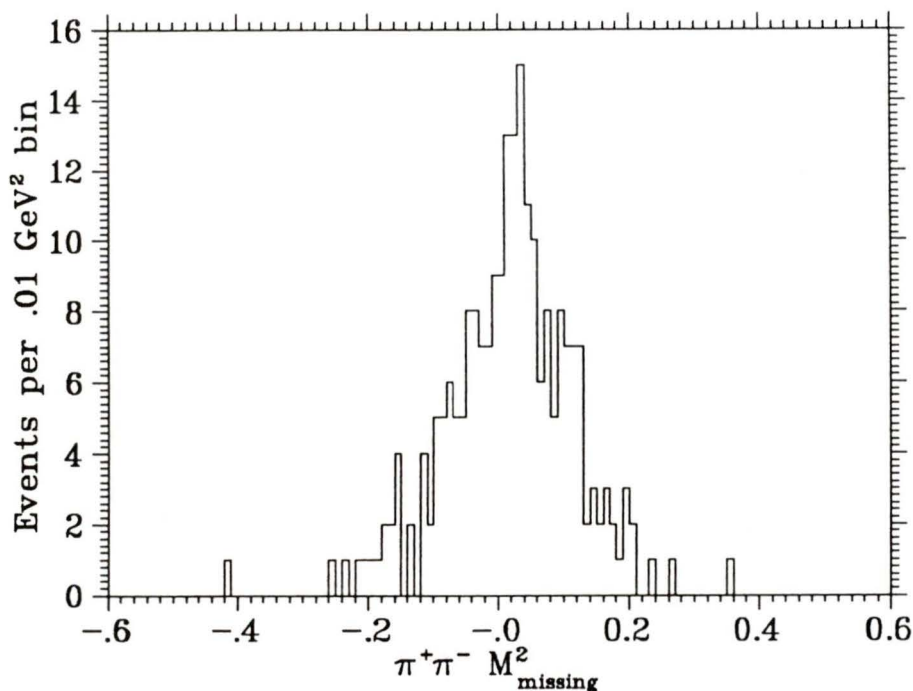


Figure 5.13: $(M^2_{missing})_{\pi^+\pi^-}$ distribution for events with $S_{initial} \geq 1.6$

a graphic illustration of the resolution, it is useful to look at plots which show how much the charged-particle momenta are “adjusted” by the fitting routine. Figures 5.14, 5.15 and 5.16 show the total charged-particle energies before and after fitting for events with $\chi^2 \leq 100$, 30 and 10, respectively. These figures illustrate how the χ^2 cut eliminates those events for which the adjustment of the charged-particle momenta is too great. Also, the fact that the bands of fit events are wider at higher energies is an indication of the property of the momentum resolution increasing with increasing charged-particle momentum.

It was subsequently discovered that the principal cause of the poor resolution was that one of the detector chambers was misaligned and slightly deformed. However, it was possible to remedy this by introducing appropriate corrections into the tracking programme. This procedure (currently in progress) has improved the resolution to a level such that it now compares

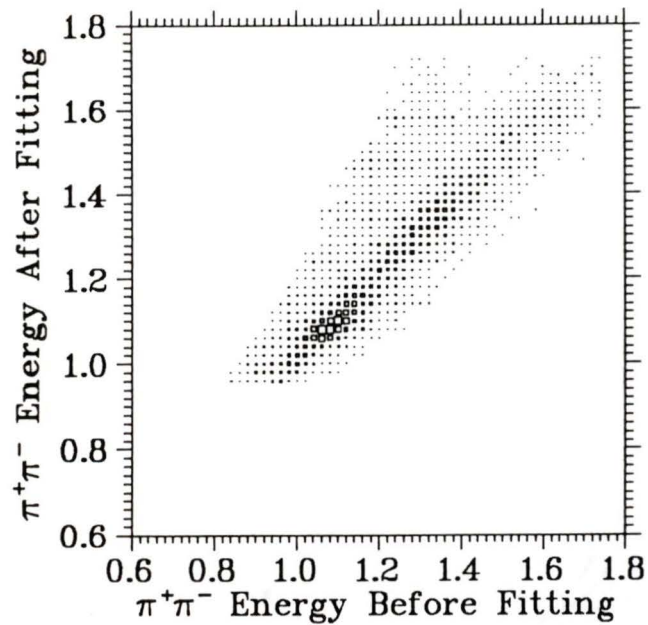


Figure 5.14: Charged-particle energy before and after fitting ($\chi^2 \leq 100$)

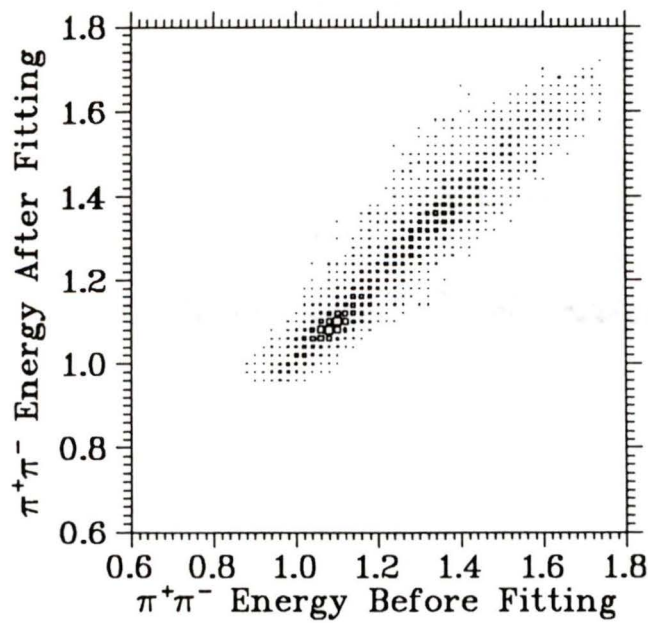


Figure 5.15: Charged-particle energy before and after fitting ($\chi^2 \leq 30$)

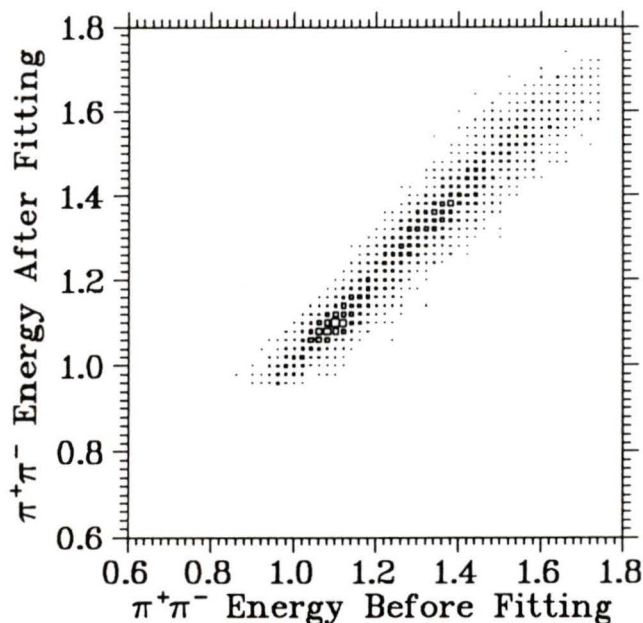
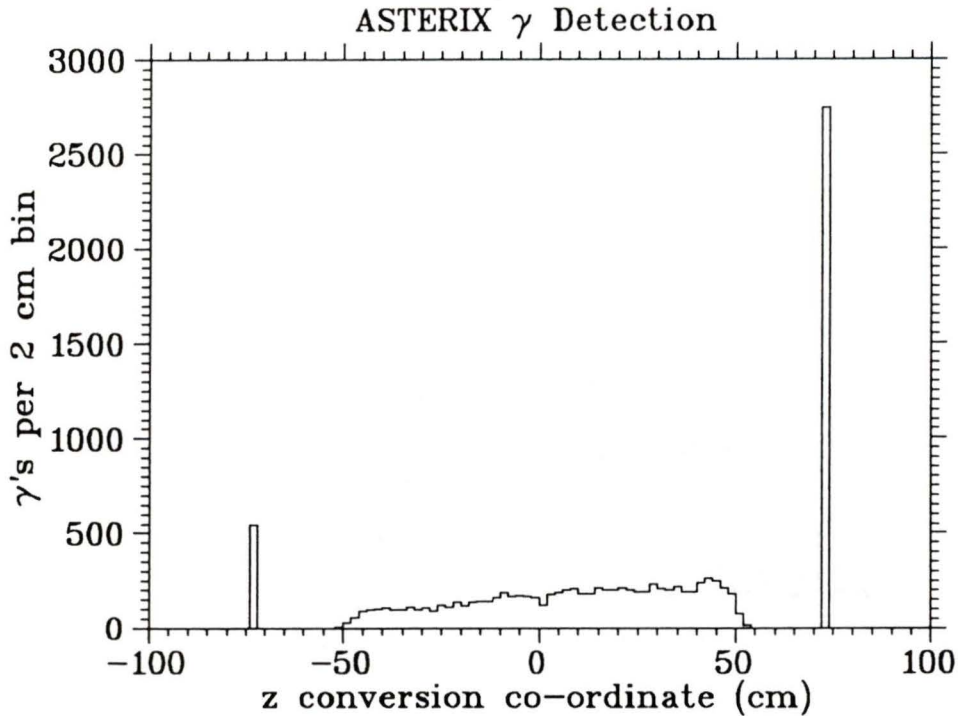


Figure 5.16: Charged-particle energy before and after fitting ($\chi^2 \leq 10$)

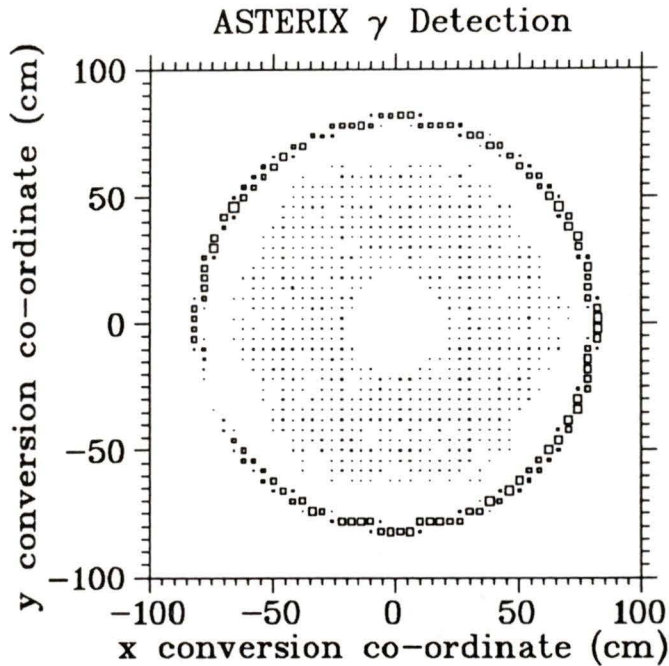
very favorably with the resolution obtained in the previous bubble chamber experiments. Unfortunately, the new, improved data was not available in time for this analysis.

The γ detection distribution for the fit events has the general features that would be expected for the given vertex distribution: it is weighted towards the downstream end of the detector, in both the cylindrical and endcap detectors (Figure 5.17). More than 2/3 of all the γ -rays were detected in the cylindrical region. This can be seen to be due to the fact that the charged prong detection is more efficient and has better resolution when the plane of the event is close to the transverse plane of the detector, so that the γ -rays from these events will also tend to be weighted toward the transverse plane. The distribution as seen in the x - y plane (i.e. in an end on view of the detector, Figure 5.18) shows several areas that could be "dead spots", i.e. regions of the detectors where the efficiency is very low

Figure 5.17: γ -ray z conversion distribution

or even nonexistent. Because of the relatively low number of γ -rays in the endcaps, the empty or near-empty regions here are probably statistical in nature, whereas the major hole in the cylindrical distribution is most likely an actual dead spot. It is often very difficult to determine how such a dead spot might bias the results without an accurate Monte Carlo simulation programme. As the $\pi^+\pi^-\pi^0$ events should be isotropic in the x - y plane it might be reasonable to assume that this dead spot would not introduce a significant bias, but only reduce the total number of events in the final data set.

It was mentioned previously that the fitted events were (for part of the analysis) divided on the basis of whether or not there was an X-ray detected. Only 671 of 5707 fitted events were found to have a genuine X-ray, as determined by the tracking programme. Since 40% of the raw events were selected by the X-ray trigger, this seems somewhat surprising.

Figure 5.18: γ -ray x - y conversion distribution

It would appear to indicate that either the X-ray trigger is not very efficient at selecting genuine X-ray candidates, or that the tracking programme does not recognize X-rays from among very well from among the possible candidates.

5.6 Physics Results

What can we learn from studying the $\pi^+\pi^-\pi^0$ final state? The area of most interest is to determine the different contributions to this state from among the possible initial states of the $\bar{p}p$ system, and also to determine the production rates of the different intermediate resonant states. Three quantum numbers are needed to specify the initial state of the $\bar{p}p$ system (neglecting the principal quantum number n): l , the orbital angular momentum quantum number; s , the spin quantum number; and I , the isotopic spin (isospin) quantum number.

It is convenient when discussing hadronic interactions to use the G -parity quantum number⁴, as this is conserved by the strong interaction. The G parity makes it somewhat simpler to apply the selection rules for the possible transitions between initial and final states.

The G parity of an $n\pi$ system is simply $(-1)^n$, so for the $\pi^+\pi^-\pi^0$ final state $g = -1$. For the $\bar{p}p$ system we have $G = (-1)^{l+s+I}$, so for G parity to be conserved it is necessary that the sum of $(l + s + I)$ be an odd integer⁵.

Considering $l = 0$ and $l = 1$ initial states only, as the vast majority of $\bar{p}p$ systems decay from one of these two states, we can list the possible initial, intermediate and final states that are allowed by the conservation rules. The proton and antiproton both have $s = 1/2$ and $I = 1/2$, but have opposite third components of both quantum numbers. The addition of both these quantities, according to the Clebsch-Gordan rules, can result in a combined total of $s = 0, 1$ and $I = 0, 1$. The $s = 1$ ($I = 1$) state has three-fold degeneracy (triplet state), while the $s = 0$ ($I = 0$) state has no degeneracy (singlet state). With the different possible values of s and l , the total angular momentum can be $J = 0, 1, 2$. In spectroscopic notation, systems with spin s and total angular momentum J are designated by $^{2s+1}S_J$ and $^{2s+1}P_J$, for orbital angular momentum $l = 0$ and $l = 1$, respectively. Table 5.2 summarizes the initial and the possible intermediate states for which G parity is conserved. The values of l in the table refer to the relative angular momenta between the dipion resonances and the third pion. The 0^{++} resonance refers to a possible resonance with spin 0, and positive parity and charge conjugation quantum numbers. The known candidates with these quantum numbers are the $f_0(975)$, the $f_0(1300)$ and the $f_0(1590)$ ⁶

⁴ $G \equiv CR$, where C is the charge conjugation operator, and R is the operator that rotates the system by 180° about the y -axis in isospin space.

⁵There is one case for which this does not hold, and that is for the electromagnetic decay $\omega^0 \Rightarrow \pi^+\pi^-$ from the $\omega^0\pi^0$ intermediate state; both the ω^0 and π^0 have $G = -1$, so that intermediate state must have come from an initial $G = 1$ $\bar{p}p$ state.

⁶This is not a well-established resonance, and according to the **Review of Particle Properties** (1986 edition) [20] has only been seen in one experiment. As well, the $\pi^+\pi^-$

Initial $\bar{p}p$ State $(2I+1)(2s+1)l_J$	Possible Intermediate Resonances			
	$\rho^0\pi^0$	$\rho^\pm\pi^\mp$	$f_2^0(1270)\pi^0$	$0^{++}\pi^0$
$^{13}S_1$	$l=1$	$l=1$	—	—
$^{31}S_0$	—	$l=1$	$l=2$	$l=0$
$^{11}P_1$	$l=0$	$l=0$	—	—
$^{33}P_0$	—	—	—	—
$^{33}P_1$	—	$l=0$	$l=1$	$l=1$
$^{33}P_2$	—	$l=2$	$l=1$	—

Table 5.2: G -parity conserving initial and intermediate states

resonances. There is no clear evidence for any of these resonances being present, although the two higher mass resonances are very broad, which would tend to make them difficult to observe even if they are present. It is quite conceivable that three resonances with identical quantum numbers that “share” two decay channels (which combined account for only a small proportion of the total $\pi^+\pi^-\pi^0$ final state [19]) would be very difficult to extract from the data, even if the statistics were significantly greater. To add to the difficulty, the $f_0(1300)$ would almost completely overlap with the $f_2(1270)$.

As well as the resonant states listed in Table 5.2 there are also the possibilities of non-resonant $\pi^+\pi^-\pi^0$ production from all of the initial states, and G -parity non-conserving $\omega^0\pi^0$ intermediate states. It would be desirable to perform a full amplitude and phase analysis on the data set in order to find the relative contributions of the different initial and intermediate states to the final $\pi^+\pi^-\pi^0$ state. Although such an analysis is beyond the scope of this thesis, we can again discern certain of the more prominent features from a qualitative analysis of the fit data. In order to do this we would like to be able to display the data in a form that allows us to “see” the various resonances produced in the annihilation process.

decay mode has not been observed.

5.7 Dalitz Plots

In an experiment such as ASTERIX we do not study the dynamics of the reactions directly; we must infer the dynamical properties of the processes under investigation from their effects on the *kinematical* properties of the final states, in this case $\pi^+\pi^-\pi^0$. Speaking in general terms, the probability for the transition from a given initial state to a given final state can be written as a product of two terms, one of which describes the dynamics of the process (sometimes called the “matrix element” for the transition), and the other which describes the kinematics (usually referred to as the “phase space”). It is almost always the case in particle physics experiments that the dynamical term is the “unknown” quantity. The phase space term can almost always be calculated, at least for relatively simple systems, as it is independent of the specific dynamical processes under investigation, and the actual probability of the transition is generally derivable directly from the experimental measurements. It is in this way that we can obtain insights into the fundamental processes which produce the observed results.

In this analysis we make use of a fundamental property of the phase space, which is known as the property of uniform density of states. What this means in the present case is that for “pure” phase space, i.e. neglecting all dynamical properties, the probability of the $\pi^+\pi^-\pi^0$ system being in any of its possible states is equal. By “possible states” is meant any configuration for which momentum and energy are conserved. This is an extremely powerful theorem, because when we examine the kinematical statistics of the $\pi^+\pi^-\pi^0$ final state, any deviation from this uniform density is attributable to the dynamical properties of the annihilation process. The Dalitz plot is a graphical technique which enables us to examine and quantify the deviations from pure phase space.

If we ignore the orientation of the system (which is justified because neither the protons nor the antiprotons are polarized, and the annihilations

occur at rest), the kinematics of the $\pi^+\pi^-\pi^0$ final state can be described by two independent variables. There are a number of possible choices as to which pair of variables we use: two of the energies (either total or kinetic); the magnitudes of two of the momenta; the relative angles between the directions of the particles; the invariant masses of any two pairs of particles. All of this information is derivable from any of the two variables chosen. The Dalitz plot uses the squares of the invariant masses of pairs of pions, because the pure phase space plot is flat (i.e. has uniform density), whereas the plot of the invariant masses themselves is not⁷. Resonances that decay to a pair of pions appear as bands of enhanced density perpendicular to the axis of the dipion invariant mass squared (M_{inv}^2); resonances of the dipion pair *not* on either of the axes appear as bands running at oblique angles to the axes.

The density of a given resonant band is not necessarily constant across the whole plot; it is a function of the spin and parity of the given resonance; these density functions (or “dynamical factors”) can be expressed as functions of the relative momenta of the particles. The phase and amplitude analysis consists of a two-dimensional fit of all of the possible resonant states to the experimental Dalitz plot.

This is not a trivial problem; the results of such a fit are highly sensitive to any kind of non-uniformity in the plot, whether it is an actual resonance, background or even statistical deviation due to a lack of data. For reliable results one needs to have a detailed knowledge of the possible biases that the detection system can introduce in the density distribution, as well as a knowledge of the distribution of background events. It is usual to try to simulate the background and detector biases with either a Monte Carlo programme or some actual events that can “mimic” the background. If the background events are more or less uniformly distributed across the plot they will cause little problem if the magnitude of the background is known.

⁷The energies could equally well serve the same purpose, as they are related to the squares of the invariant masses by a linear transformation.

Another useful property of the Dalitz plot in this instance is the symmetry (provided charge conjugation holds) between the π^+ and π^- . This allows us to fold the plot over, thereby effectively doubling the amount of data available. This adds considerably to the statistical reliability of the results.

The first reliable attempt at such an amplitude-phase analysis [14] found (not surprisingly) all of the events to have come from either the 3S_1 (84%) and 1S_0 (16%) states. While the former figure is probably reliable, the latter is unreliable because of the large background, estimated at $(14 \pm 3)\%$. Because the background is considerably larger than the calculated non-resonant 1S_0 term, it would be virtually impossible to discern any 0^{++} resonance from amongst the noise, if indeed there was one.

Such would not be the case with the 3C-fit data set. With so little background present and almost 50% more events⁸, a much more definitive statement could be made on the presence (or non-presence) of a 0^{++} resonance.

One obvious qualitative observation that can be made from the 3C data is the increased presence of the f^0 ⁹. The above-mentioned analysis found f^0 production to account for only 4% of the total, and indeed the f^0 resonance is just barely discernable on their Dalitz plot (Figure 5.19). Our Dalitz plot (Figures 5.20) shows a much greater f^0 presence. If their results for the relative amplitudes of the 1S_0 and 3S_1 states are at all reliable, it means that our Dalitz plot must have a significant proportion of P-wave $\bar{p}p$ annihilations. This would certainly be expected from annihilations in gaseous, as opposed to liquid, hydrogen.

There are some features of the Dalitz plot that can be traced to limitations in the detection system. The “bites” out of the corners near where

⁸This is before the retracking of the data, which could increase the data sample by a factor of three.

⁹When speaking of the “ f^0 ”, we are referring to the $f_2(1270)$ resonance, where the subscript denotes the spin of the particle, and the superscript represents the charge.

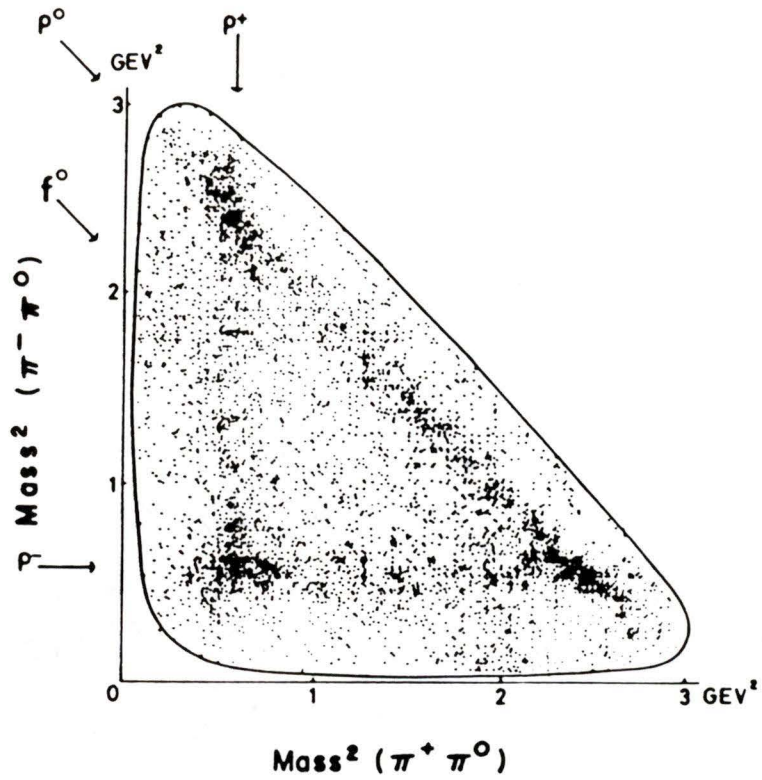


Figure 5.19: Dalitz plot from bubble chamber data

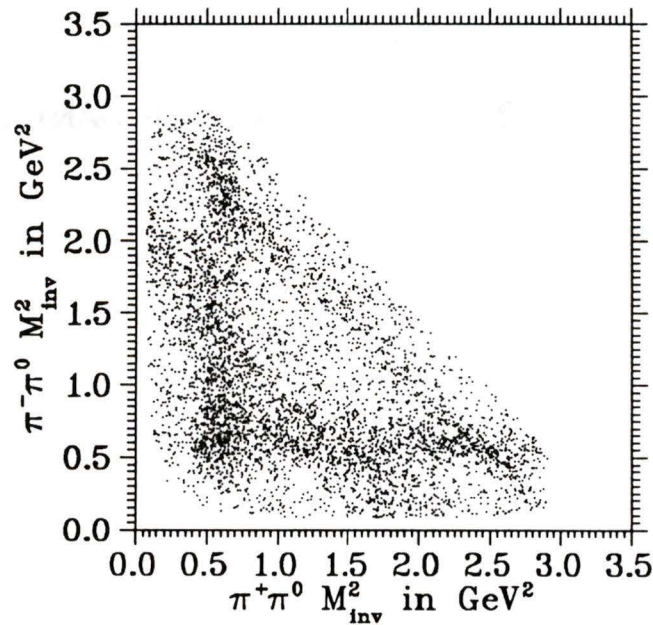


Figure 5.20: Dalitz plot from ASTERIX 3C fit

the charged and neutral ρ bands overlap are due to the lower-momentum limit for charged particles. Similarly, there is a paucity of events in the corner near where the two charged ρ bands overlap, attributable to a relative inefficiency of the γ detection system to detect low-energy photons.

A feature that can readily be explained by the misalignment of the chambers is an asymmetry in the number of events lying above and below the diagonal line in the $(M_{inv}^2)_{\pi^+\pi^0}$ v. $(M_{inv}^2)_{\pi^-\pi^0}$ plot. There are 211 more events above the diagonal than below it. This corresponds to a higher mean and median value of negative momentum (630 and 693 MeV/c, respectively) than positive momentum (623 and 683 MeV/c, respectively), which in turn is entirely consistent with a slight misalignment of one of the chambers. Such a misalignment would consistently overestimate one curvature and underestimate the other.

5.8 Invariant Mass Plots

The invariant mass plots are simply the projections of the Dalitz plots onto the axes. A weak resonance (i.e. one that enhances the density of the Dalitz plot only slightly) would show up more clearly in such a plot, as the entire band would be added. A comparison of the $(M_{inv}^2)_{\pi^+\pi^-}$ plot from the 3C fit with the same plot from the bubble chamber data (Figure 5.21 and Figure 5.22 (bottom), respectively) clearly shows the enhanced production of the f^0 in the ASTERIX data. The 3C fit plots of $(M_{inv}^2)_{\pi^+\pi^0}$ and $(M_{inv}^2)_{\pi^-\pi^0}$ (Figures 5.23 and 5.24, respectively) show a larger peak-to-background ratio than either the 1C bubble chamber data (Figure 5.22 (top)) or the ASTERIX 1C data, which is indicative of the greatly reduced background achieved by the 3C fit. This reduced background is also evident in the comparison of the $(M_{inv}^2)_{\pi^+\pi^-}$ plots for the ASTERIX 3C and 1C fits.

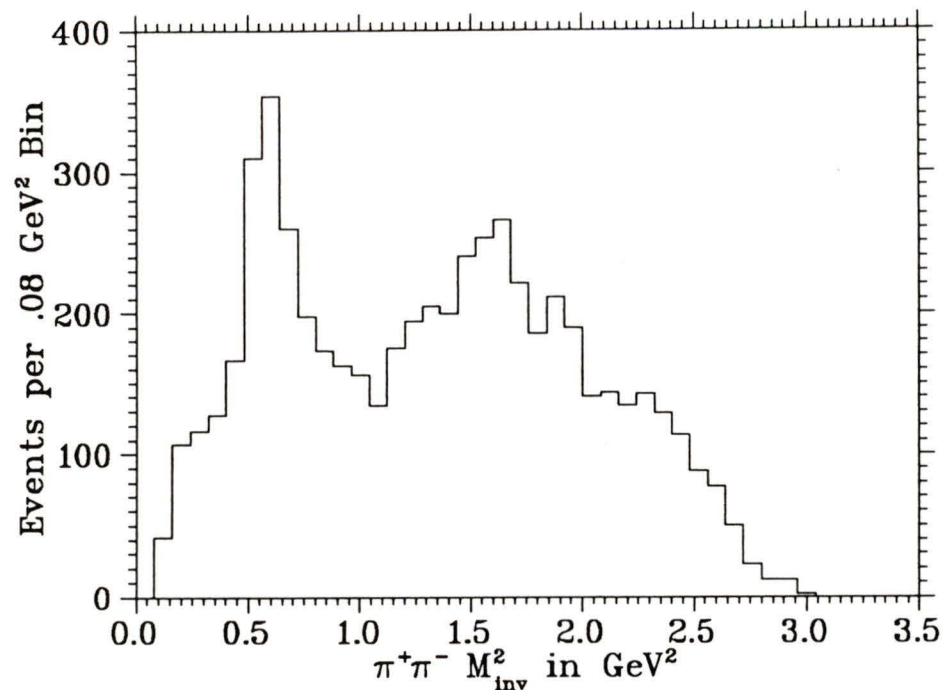
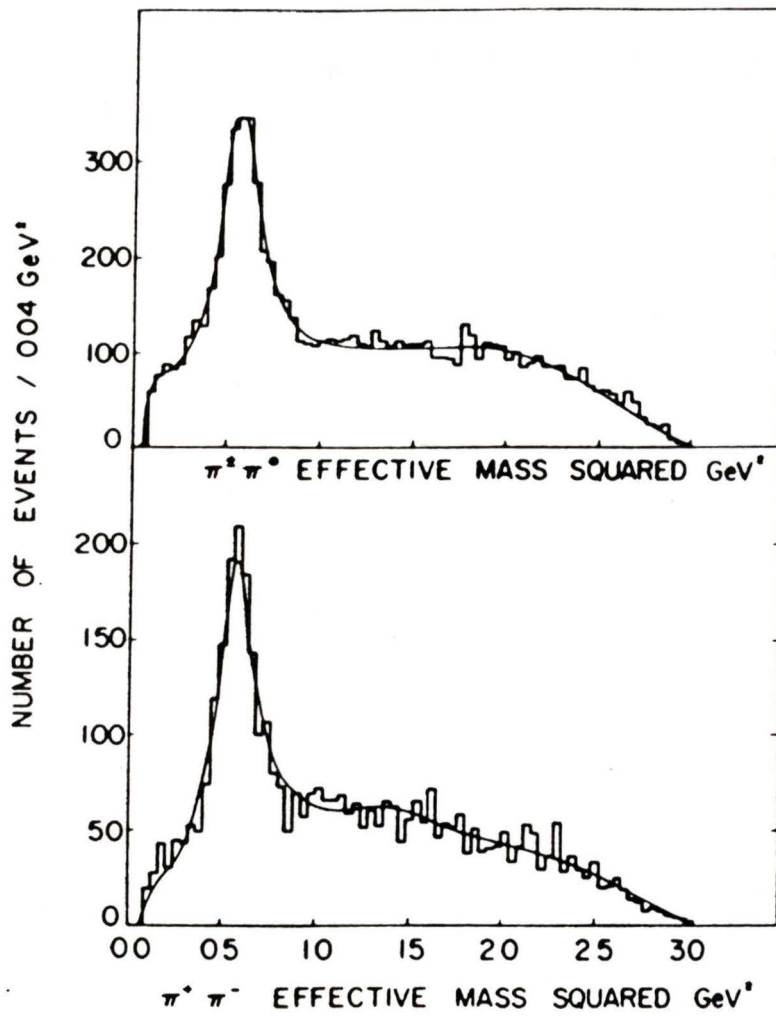
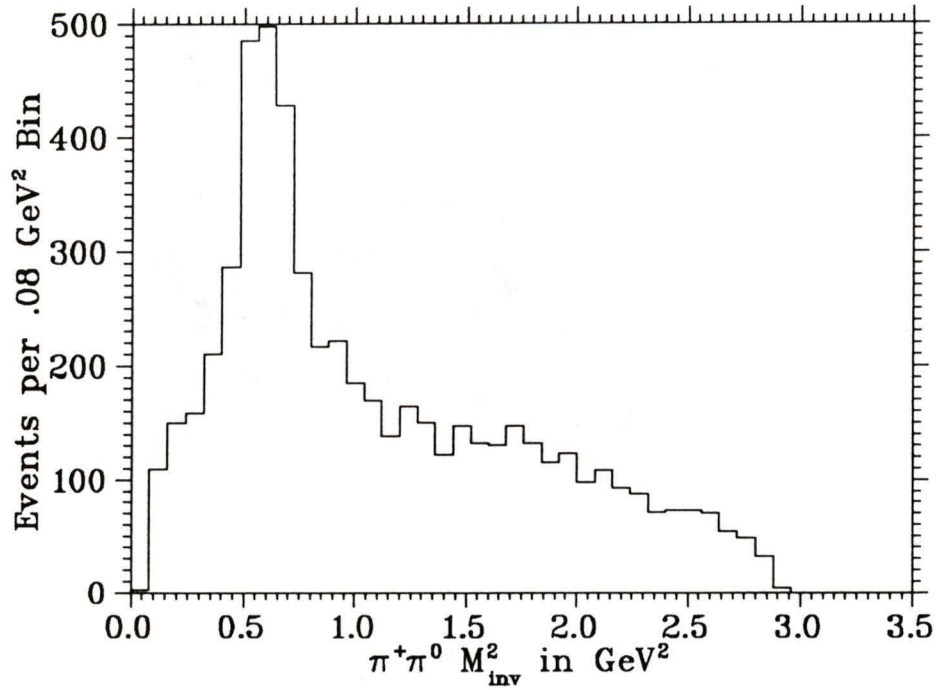
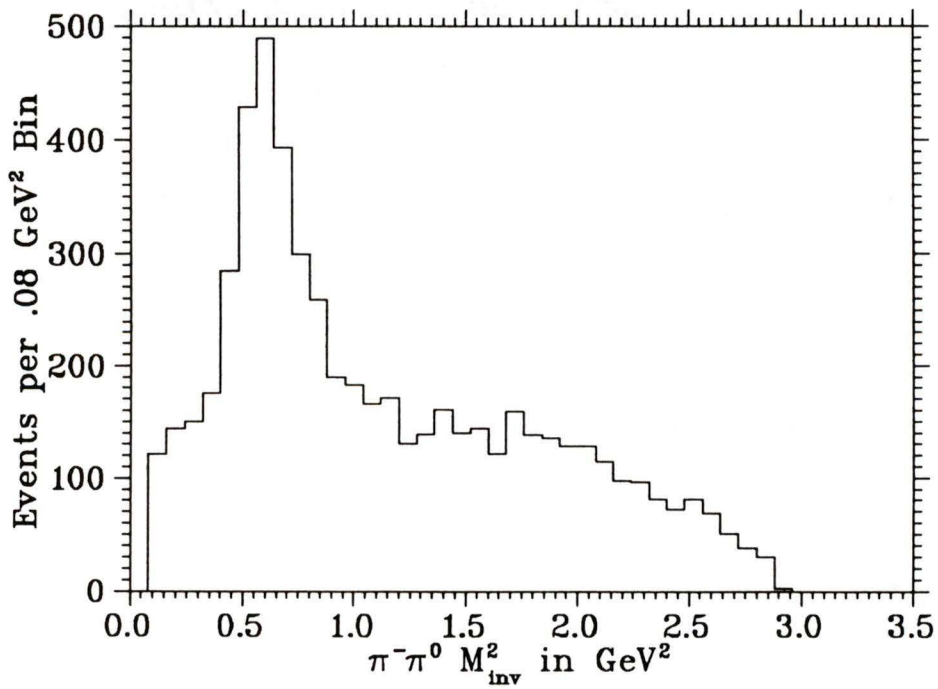


Figure 5.21: $(M_{inv}^2)_{\pi^+\pi^-}$ from ASTERIX 3C data

5.9 Angular Distributions

The Dalitz plot data can also be manipulated to obtain the angular distributions for the decays of resonances (as measured in the rest frame of the dipion). These distributions are dependent on the various dynamical factors that weight the density functions of the resonance, but generally are only useful as part of a complete amplitude and phase analysis. This is because the angular distribution for a given resonance will often be completely dominated by peaks corresponding to the overlap regions of the given resonance with others on the Dalitz plot. This feature makes it very difficult to derive the relative contributions of the different dynamical factors without a complete analysis of the other resonances as well. Figures 5.25 to 5.27 show the cosine of the center-of-mass decay angle as a function of invariant mass for the positive, negative and neutral dipions, respectively. The resonance bands for the second and third dipions, in all cases, can be seen to

Figure 5.22: M_{inv}^2 plots from bubble chamber data

Figure 5.23: $(M_{inv}^2)_{\pi^+\pi^0}$ plot from ASTERIX 3C dataFigure 5.24: $(M_{inv}^2)_{\pi^-\pi^0}$ plot from ASTERIX 3C data

be curved and of non-uniform width in this type of data representation.

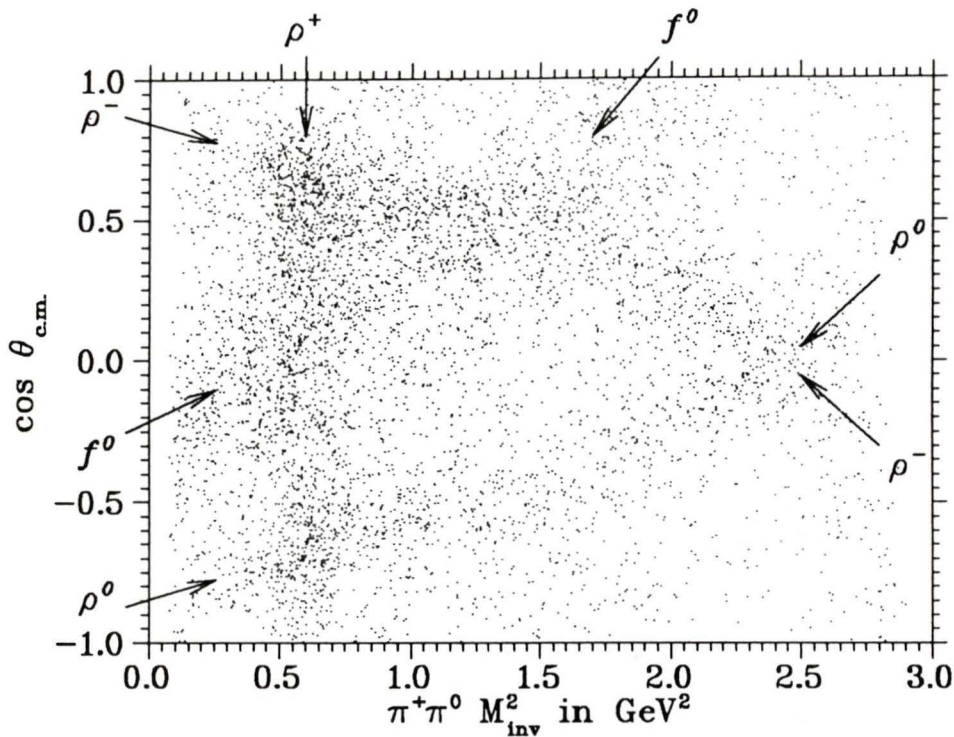


Figure 5.25: Angular distribution for positive dipion

5.10 X-ray Information

As mentioned earlier, it was intended to analyse the data based on a division of events with and without X-rays. But the number of fit events with X-rays (which could consist of up to $\approx 90\%$ P-state annihilations, based on the relative frequency of 2p and 1s annihilations) was too small (672 events) to enable any meaningful comments on this aspect. It is hoped that the ongoing retracking will produce enough clean events with X-rays to enable a complete analysis of a set P-wave enhanced 3C data.

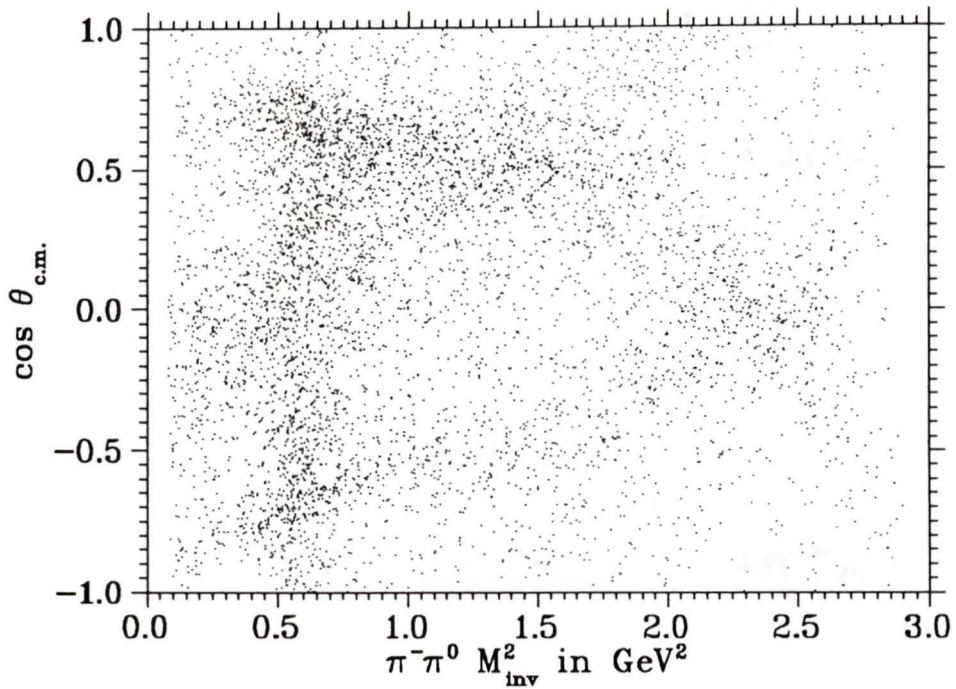


Figure 5.26: Angular distribution for negative dipion

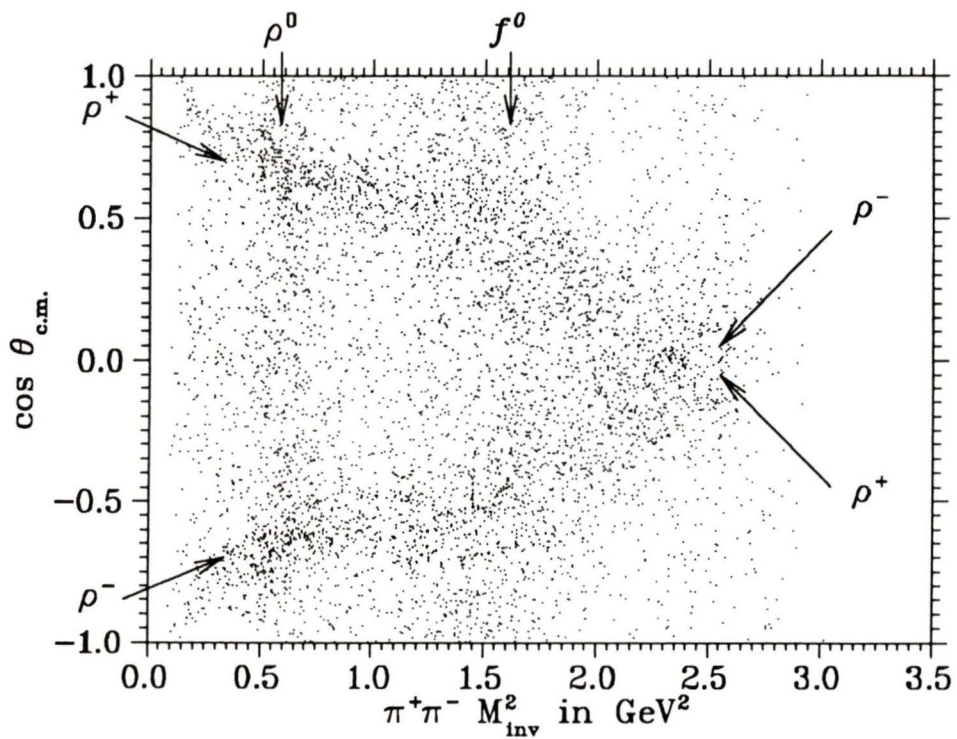


Figure 5.27: Angular distribution for neutral dipion

5.11 Further Prospects

The use of γ -ray positional information has been very effective in obtaining a clean $\pi^+\pi^-\pi^0$ signal from $\bar{p}p$ decays. The major reason for this, simply put, is that the probability of random γ -rays from non- $\pi^+\pi^-\pi^0$ events being configured in such a way to “mimic” those from a real event is very small, provided the charged-particle tracks range of correction is limited by a tight cut on the χ^2 of the fit. It has been shown that even with poor charged-particle momentum resolution it is possible to obtain an almost pure sample of $\pi^+\pi^-\pi^0$ events. This is a definite improvement over the capability of the one-constraint fitting technique.

The Monte Carlo simulation was able to provide good fits to both the complete and the fit ($\chi^2 \leq 10$) data sets. This itself should enable us to obtain preliminary values of the branching ratios for different combinations of π^0 , $2\pi^0$, $3\pi^0$, η and possibly ω , with a $\pi^+\pi^-$ pair, providing that the absolute γ -ray detection efficiency is known.

The retracked data, with improved momentum resolution, should provide at least two to three times more data, which would allow a high precision amplitude-phase analysis of a data set practically free from contamination, and also allow the above-mentioned branching ratios to be computed with much less uncertainty. A similar analysis could also be done by replacing the π^0 by the η , whose dominant decay mode ($\approx 40\%$) is into two γ -rays.

Of course, there is no reason to limit the analysis to only two charged prongs and one neutral particle; with relatively simple modifications the fitting routine could also accommodate multiple π^0 events and neutral ω^0 decays (i.e. $\omega \Rightarrow \pi^0\gamma$).

References

- [1] R. Armenteros *et al.* *A Study of $\bar{p}p$ Interactions at Rest in a H_2 Gas Target at LEAR*. CERN/PSSC/80-101 PSSC/P28. August 29, 1980.
- [2] R. Landua. *The Atomic Cascade in $\bar{p}p$ and Implications for $\bar{p}p$ Annihilations at Rest* in **Physics at LEAR with Low-Energy Cooled Antiprotons** (eds. U. Gastaldi and R. Klapisch). Plenum Press, New York, 1984.
- [3] J. Bailey *et al.* Phys. Lett. **33B** (1970) 369.
- [4] B. Budick, J.R. Toraskav and I. Yaghoobia. Phys. Lett. **34B** (1971) 539.
- [5] M. Leon and H.A. Bethe. Phys. Rev. **127** (1962) 636.
- [6] E. Auld *et al.* Phys. Lett. **77B** (1978) 454.
- [7] E. Jones. *The CERN \bar{p} Complex and Present Status and Future Developments of the Antiproton Accumulator* in **Physics at LEAR with Low-Energy Cooled Antiprotons** (eds. U. Gastaldi and R. Klapisch). Plenum Press, New York, 1984.
- [8] P. Lefèvre. *Construction of the LEAR Facility: Status Report* in **Physics at LEAR with Low-Energy Cooled Antiprotons** (eds. U. Gastaldi and R. Klapisch). Plenum Press, New York, 1984.
- [9] S. Ahmad *et al.* Phys. Lett. **157B** (1985) 333.

- [10] S. Ahmad *et al.* *Protonium Spectroscopy and Identification of P-wave and S-wave Initial States of $\bar{p}p$ Annihilations at Rest with the ASTERIX Experiment at LEAR* in **Physics at LEAR with Low-Energy Cooled Antiprotons** (eds. U. Gastaldi and R. Klapisch). Plenum Press, New York, 1984.
- [11] J.M. Richard. *Protonium and Other Exotic \bar{p} -Atoms* in **Physics at LEAR with Low-Energy Cooled Antiprotons** (eds. U. Gastaldi and R. Klapisch). Plenum Press, New York, 1984.
- [12] R. Bizzarri. *Nucleon-Antinucleon Annihilation at Low Energies* (review article) in **Physics at LEAR with Low-Energy Cooled Antiprotons** (eds. U. Gastaldi and R. Klapisch). Plenum Press, New York, 1984.
- [13] C.B. Dover, J.M. Richard and M.C. Zabek. *Ann. of Phys.* **130** (1980) 70.
- [14] M. Foster *et al.* *Nucl. Phys.* **B6** (1968) 109.
- [15] D. Axen. *An Amplitude Analysis of $\bar{p}p \Rightarrow \pi^+\pi^-\pi^0$* . ASTERIX internal document. 1987.
- [16] R.K. Bock and J. Zoll. *Principles of the GRIND Kinematic Fit*. CERN Computer 6000 Series Program Library Long Write-up X 601. 1967.
- [17] C. Amsler. *CINEMA: A Program to Fit Events in the ASTERIX Experiment*. ASTERIX internal document. 1982.
- [18] L. Lyons. **Statistics for Nuclear and Particle Physicists**. Cambridge University Press, New York, 1986.
- [19] C. Amsler. *$\pi^+\pi^-\pi^0$ Summary*. ASTERIX Note 101. ASTERIX internal document. 1984.

- [20] M. Aguilar-Benitez *et al.* (Particle Data Group). Phys. Lett. **170B**
(1986) 22.

Vita

Surname: **Mildenberger**

Given Names: **Joseph Lloyd**

Place of Birth:

Regina, Saskatchewan

Date of Birth:

September 19, 1961

Educational Institutions Attended:

University of Victoria, B.C.

1979 to 1984

University of Victoria, B.C.

1985 to 1987

Degrees Awarded:

B.Sc. (Honors) 1984

University of Victoria

Honors and Awards:

NSERC Summer Student Bursary


1981

Partial Copyright License

I hereby grant the right to lend my thesis (the title of which is shown below) to users of the University of Victoria Library, and to make single copies only for such users, or in response to a request from the library of any other university or similar institution, on its behalf or for one of its users. I further agree that permission for extensive copying of this thesis for scholarly purposes may be granted by me or a member of the university designated by me. It is understood that copying or publication of this thesis for financial gain shall not be allowed without my written permission.

Title of Thesis:

**USE OF PHOTON DETECTION TO OBTAIN
A CLEAN $\pi^+\pi^-\pi^0$ SIGNAL
FROM $\bar{p}p$ ANNIHILATIONS**


Author Joseph Lloyd Mildenerger

August 28, 1987